ANALYSIS OF EFFECT OF POROSITY ON THE DISCHARGE OF SILICON-AIR BATTERY

by

Siri Gani

in partial fulfilment of the requirements for the degree of

Master of Science in Sustainable Energy Technology
at the Delft University of Technology,
to be defended publicly on Monday, 27 September 2021, 10.30 hrs.

Thesis Committee:
Dr. René van Swaaij (chair and supervisor)
Dr.ir. Rudi Santbergen
Dr. Erik van der Kolk

ABSTRACT

Energy storage is a critical component in decreasing the unpredictability of renewable energy. Silicon-air battery is a type of storage technology that potentially has a higher energy density than lithium-ion battery. The silicon-air battery, on the other hand, must overcome corrosion and passivation reactions in order to discharge continuously. One method of reducing the passivation reaction is by increasing the dissolution rate of the discharged product higher than its generation rate. This is possible by increasing the surface area of silicon anode by making it porous. The objective of this research is to evaluate the effect of porosity on the discharge of a silicon-air battery. In this work amorphous silicon (a-Si:H) based anodes made by Plasma Enhanced Chemical Vapor Deposition (PECVD) technique are used. The deposition power and deposition pressure are altered to obtain a-Si:H anodes of different porosities. The influence of these deposition conditions on porosity and conductivity is studied. In order to find the porosity, the refractive index of the deposited a-Si:H layer was obtained from optical characterization. Bruggeman's Effective Medium approach is followed to calculate porosity. The deposition power has the greatest impact on the refractive index, porosity, and conductivity of the a-Si:H layer. Increasing the deposition power raises the porosity and the conductivity. This thesis also looks into the effect of varying the fraction of dopant gas in the gas mixture on porosity and conductivity. The experiments show that both porosity and conductivity increase with higher fraction of dopant gas. The deposited a-Si:H layer and c-Si wafer were used as anode in the discharge of silicon-air battery.

CONTENTS

LIST OF FIGURES

LIST OF TABLES

ACRONYMS

1 INTRODUCTION

The industrial revolution triggered the burning of fossil fuels such as coal, natural gas and oil. Increased human activity has accelerated the carbon emissions caused by the burning of these fossil fuels. These changes have resulted in climate change that can be dangerous to human life. Several international treaties, such as the Kyoto Protocol and the Paris Agreement, have been established to address this issue [31] [1]. To reach the focused purpose of these treaties, fossil fuels are being superseded by renewable energy sources to reduce greenhouse gases. The most commonly used renewable sources are sun and wind as they are inexhaustible. However, generating electricity from solar and wind energy cannot be predicted very well and is intermittent. Because the sun does not shine all day and the wind does not blow all the time, there is a mismatch between the generation and consumption of energy. Any excess energy produced should be stored and used when these resources are unavailable. As a result, energy storage becomes an enabler technology, reducing the intermittency and unpredictability of solar and wind resources. Furthermore, energy storage bridges the demand-supply gap, reduces the need for backup power plants, and reduces greenhouse gas emissions [36].

Hydropower pumped storage, compressed air energy storage, flywheels, flow batteries, lead-acid batteries, lithium-ion batteries, metal-air batteries, and more energy storage methods are available [2]. The benefits of adopting battery technology for energy storage are its extended lifetime, high efficiency, and quick construction time. Out of all the battery options, lithium-ion batteries are preferred because of their high energy density and lightweight. The availability of lithium and cobalt is seen in Fig 1.1. Because the world's supply of lithium and cobalt is limited, the earth would eventually run out of the metals required for lithium-ion batteries [49]. The problem with cobalt mining, which is used in lithium-ion batteries is that the Republic of the Congo breaches human rights by exploiting child labor and not providing reasonable wages [68].

Another form of battery technology known as metal-air batteries is an appealing alternative to lithium-ion batteries since it employs pure metal as the anode and oxygen from the atmosphere as the cathode [52]. The metal-air battery is light in weight due to the absence of a cathode, which contributes to a high gravimetric energy density and volumetric energy density [11]. Furthermore, there is a cost reduction, and the anode employed in metal-air batteries except lithium is abundant in nature. Metal-air batteries containing metals such as lithium, iron, magnesium, aluminum, zinc, calcium, potassium, and sodium have been studied. Metal-air batteries also

employ semiconductor metals like germanium and silicon. Commercially available metal-air batteries include zinc-air batteries and aluminum-air batteries [11].

In Fig 1.2, the energy densities of several metal-air batteries are compared to those of a lithium-ion battery and gasoline [66].

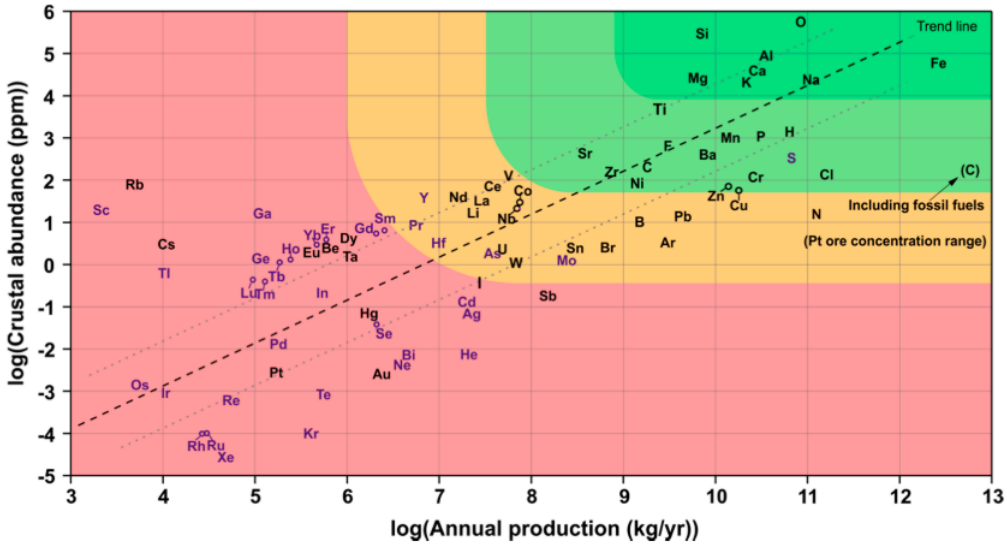

Figure 1.1: The availability of elements on earth. Silicon and oxygen are available in abundance when compared to lithium and cobalt. Image taken from [66].

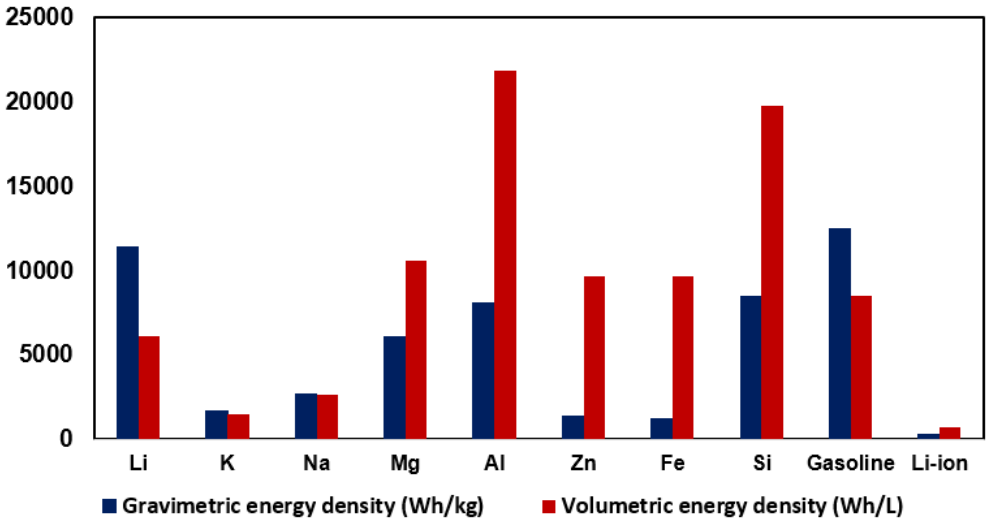

Figure 1.2: Theoretical gravimetric and volumetric energy densities of different metals in metal-air batteries in comparison with Li-ion battery and gasoline. Image adapted from [66].

Silicon has a larger volumetric energy density than lithium-ion batteries, gasoline, and other metal-air batteries except for aluminum, as well as a higher gravimetric energy density than all metal-air batteries except lithium.

Fig 1.1 highlights the silicon air battery, which is the second most abundant element on the planet. When compared to lithium, both silicon and oxygen are abundant.

The silicon-air battery was first studied by Gil Cohn and Yair Ein-Eli in 2009 at the Technion-Israel Institute of Technology [15][17][58][14][16][13]. This research was further followed by Zhong et al. in 2012 [74], Garamoun et al. in 2014 [25], Park et al. in 2015 [48] and Durmus et al. in 2017 [19] who demonstrated the necessity to overcome passivation and corrosion reactions that impede silicon-air battery discharge.

1.1 OPERATION OF THE SILICON–AIR BATTERY

In order to define the problem focused in this thesis, the operation of silicon-air battery and the factors affecting the continuous discharge of the battery is described in this section.

A silicon-air battery consists of silicon anode, air cathode and (alkaline) electrolyte. The assembly of these components is presented in Fig 1.3. During the discharge process of a silicon-air battery, silicon is oxidized at the anode side and oxygen is reduced at the cathode side. Silicon, porous carbon and KOH dissolved in water represent the components anode, cathode and electrolyte, respectively.

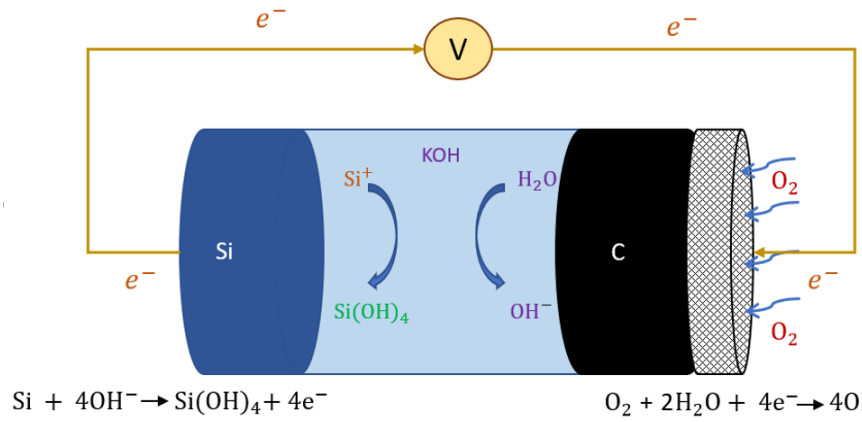

Figure 1.3: Schematic representation of a silicon-air batter with anodic and cathodic reactions. The yellow arrow indicates the direction of flow of electrons from anode to cathode.

As illustrated in Fig 1.3, at the anode, silicon from the silicon anode combines with hydroxide ions from the electrolyte to form silicic acid ($Si(OH)_4$), and 4 electrons. These electrons are released and transported from anode to

cathode through the external circuit. Silicic acid is the main reaction product formed during the discharge of the silicon-air battery.

$$Si + 4OH^- \rightarrow Si(OH)_4 + 4e^- \tag{1.1}$$

At the cathode, oxygen combines with the electrons and water from the electrolyte to reduce oxygen to hydroxide ions.

$$O_2 + 2H_2O + 4e^- \rightarrow 4OH^- \tag{1.2}$$

In the overall reaction, silicon is oxidized and oxygen is reduced to form the discharge product, silicic acid.

$$Si + O_2 + 2H_2O \rightarrow Si(OH)_4 \tag{1.3}$$

Apart from the discharge reactions mentioned above, the silicon-air battery suffers from self-discharge, which is termed as corrosion, and anodic side reaction, which is termed as passivation.

Corrosion

In addition to the discharge process, the silicon-air battery goes through a self-discharge process called corrosion [33]. This is seen in Fig 1.4. At the anode side, a fraction of electrons move towards the silicon anode surface called the temporary cathodic site instead of being transported to the external circuit [66]. At the temporary cathodic site, the electrons combine with water from the electrolyte to generate hydroxide ions and hydrogen gas. This hydrogen gas reacts with the discharge product (silicic acid) to form water and $SiO_2OH_2^{2-}$.

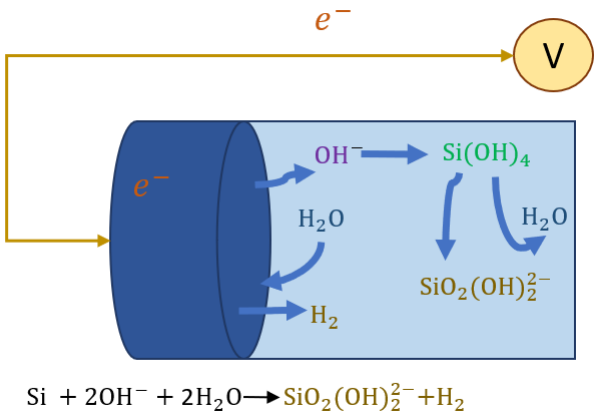

Figure 1.4: Illustration of corrosion reaction in silicon-air battery.

The reactions at the anodic site, temporary cathodic site, and the overall corrosion reaction are given by [74],

$$\text{Anodic site: } Si + 4OH^- \rightarrow Si(OH)_4 + 4e^- \tag{1.4}$$

$$\text{Cathodic site} : 4H_2O + 4e^- \rightarrow 4OH + 2H_2 \tag{1.5}$$

$$\text{Bulk electrolyte: } Si(OH)_4 + 2OH^- \rightarrow SiO_2OH_2^{2-} + 2H_2O \tag{1.6}$$

$$\text{Overall corrosion: } Si + 2OH^- + 2H_2O \rightarrow SiO_2OH_2^{2-} + 2H_2 \tag{1.7}$$

The stability of silicon in an aqueous electrolyte is illustrated by a Pourbaix diagram in Fig 1.5, where the vertical axis represents the potential and the horizontal axis represents the pH value. The dashed lines in the Pourbaix diagram represent the stability window of water. It can be seen that silicon (Si) is located outside of the stability window of water whereas SiO_2 is positioned inside the stability window of water. This means that the silicon in an aqueous electrolyte will be oxidized while also reducing the electrolyte. This reduction of the electrolyte favors the flow of electrons into the electrolyte instead of transporting via the external circuit which is an indication of corrosion reaction.

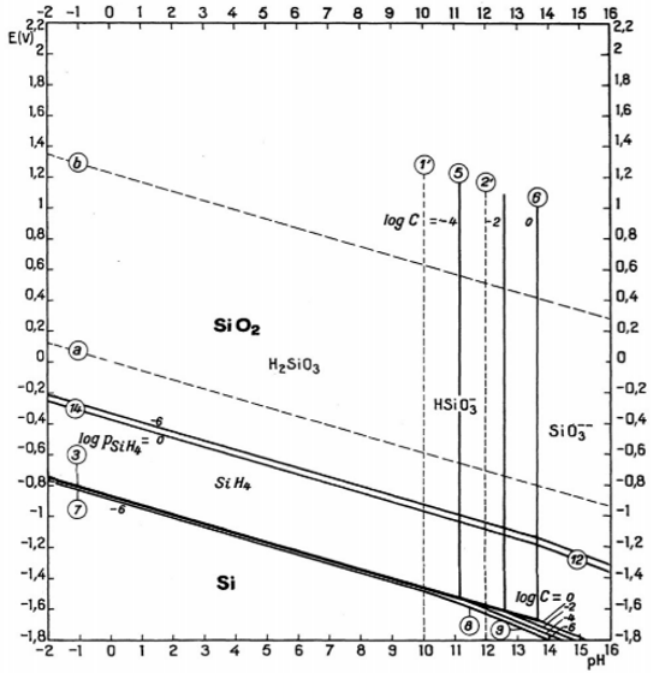

Figure 1.5: The Pourbaix diagram for silicon in aqueous solution. Dashed lines a and b represent the stability window of water. c-Si is well below the stability window and SiO_2 is inside the stability window. Image taken from [47].

Passivation

Another complication encountered by silicon-air batteries is passivation [74][48]. The discharged product, silicic acid ($Si(OH)_4$) dissolves into the electrolyte

as it is being formed. Since the $Si(OH)_4$ dissolves into the electrolyte, the concentration of this discharge product in the electrolyte is increased. This hinders further dissolution of $Si(OH)_4$ in the electrolyte. At some point, the dissolution rate of $Si(OH)_4$ is slower than the generation rate of $Si(OH)_4$, which results in the splitting of $Si(OH)_4$ into SiO_2 and H_2O. Hence, the surface of the silicon anode would be covered by SiO_2 if the dissolution rate drops below the generation rate of $Si(OH)_4$ [4]. In the Fig 1.6, the layer of SiO_2 on the anode surface is called the passivation layer. This passivation layer changes the state of the anode electrode from active to relatively inactive thus, preventing the continuous discharge.

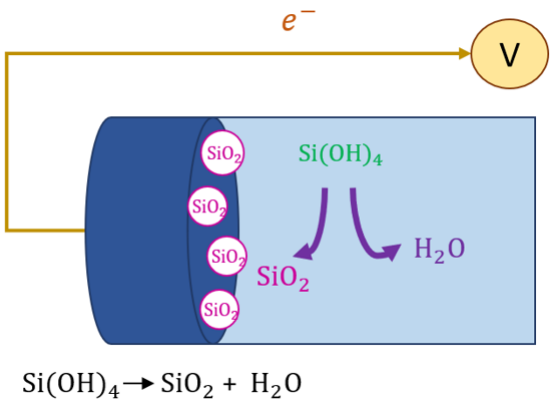

Figure 1.6: Illustration of passivation reaction in silicon-air battery.

The Pourbaix diagram in Fig 1.5 shows that SiO_2 is a stable product and hence passivates the silicon anode [66][29][5].

The passivation reaction is given below.

$$Si(OH)_4 \rightarrow SiO_2 + 2H_2O \tag{1.8}$$

Since passivation influences the depth of discharge of the battery, it is important to delay this process by either increasing the overall dissolution rate or by decreasing the rate at which the dissolution rate declines over time [51].

1.2 PROBLEM DEFINITION

Despite extensive study on silicon-air batteries, there is still a need to solve the problems that limit the discharge of silicon-air batteries, such as corrosion and passivation reaction. Corrosion refers to the self-discharge of the battery, whereas passivation refers to the blocking of the silicon anode by non-soluble discharge products, which eventually prevents silicon consumption, resulting in a short discharge period of the battery [40][70]. The corrosion reaction is reduced by using a low concentration of an alkaline solution or room temperature ionic liquid Room Temperature Ionic Liquid (RTIL) [74][64]. However, RTIL is not preferred due to safety concerns [74]. As a result, alkaline solution is commonly used in silicon-air battery research [64].

Both corrosion and passivation reactions are severe in the presence of alkaline solutions. Because silicon consumption is required for battery discharge, the passivation reaction must be postponed in order to attain high discharge capacities.

1.2.1 Need for research

The formation of a passivation layer on the anode prevents the battery from further discharge [71]. Hence, the silicon from the anode is not fully utilized. This results in reduced discharge time and discharge potential of the battery [74][48][25]. The benefit of overcoming this problem is increased discharge time and discharge potential which reflects on the specific discharge capacity. By delaying the passivation reaction the battery continues to discharge because silicon is available and ready to be consumed for the discharge reaction to occur.

According to Zhong et al., the texturing of the anode increases the specific discharge capacity of the battery by delaying the passivation reaction [74]. The research by Park et al. and Garamoun et al. also demonstrates that increasing the surface area of the anode increases specific discharge capacity [48][25]. It is apparent that expanding the surface area of the anode is a popular approach for delaying the passivation reaction, which enhances the specific discharge capacity. The passivation reaction is suppressed in this study as well by altering the structure of the silicon anode by increasing its surface area.

While Zhong et al. and Park et al. utilized c-Si as the anode, Garamoun et al. employed a-Si:H as the anode, which has a porous structure [25]. In this work we aim to investigate a-Si:H for application in a silicon-air battery. Garamoun et al. discharged the silicon-air battery by using a-Si:H anode of a fixed porosity [25]. In order to study the effect of the porosity the discharge behavior of the silicon-air battery with a-Si:H anode of varied porosity must be investigated.

The discharge performance of the battery is projected to increase by adopting a porous a-Si:H anode [73]. This improvement is due to delayed passivation, which occurs when the increase in surface area allows the diffusion of electrolyte into pores [74]. This increases the dissolution rate of the discharge product while slowing the rate of passivation.

1.2.2 Research Gap

1. *Methodological Gap:* Until now the methods used to increase the surface area of the silicon anode have been metal-assisted electroless chemical etching, electrochemical etching and PECVD [74][48][25]. Garamoun et al. used PECVD to grow a-Si:H film by using a fixed set of deposition parameters. In a PECVD process, the structure of the film is modified as the film is being grown whereas, in other methods, the anode structure

is modified separately before the discharge of the battery [25]. However, the porosity of the film can be altered by adjusting the deposition parameters such as temperature, power, and pressure [30]. Among these options, PECVD is preferred because the film can be grown at low temperature, a variety of film structures can be obtained by varying the deposition conditions and it provides uniform growth [41]. Deposition parameters such as power and pressure are modified to create different porosites to study the influence of deposition conditions on the porosity of the film. **Therefore, this research attempts at filling the gap between the numerous known approaches for increasing anode surface area and illustrates the effect of PECVD deposition parameters on porosity.**

2. *Knowledge Gap:* A knowledge gap exists due to a lack of clarity in the discharge behavior of silicon-air batteries using a-Si:H as the anode of varying porosities. The battery performance of a c-Si anode with increased surface area and an a-Si:H anode with fixed porosity is well understood [74][48][25]. However, the performance of the battery varies as the porosity is varied because of the difference in the surface area of the silicon anode. **Through this research, the discharge curve of silicon-air battery using a-Si:H anode of various porosities is studied.**

3. *Evaluation Gap:* Previous research has revealed the optical and electrical properties of silicon anodes. These properties, however, are not measured in silicon-air batteries using a-Si:H as the anode. In this study we intend to investigate the dependence of the performance of silicon-air batteries on the porosity. The porosity is assessed by using a model, which is based on optical constants. These characteristics aid in a better understanding of the behavior of the anode during discharge. In addition, the impact of doping on porosity is investigated. To determine the effect of doping on porosity, the dopant concentration is also altered by changing the fraction of dopant gas in the reaction chamber. **The current study examines the optical properties as a means to find porosity of a-Si:H anode, as well as the effect of doping and dopant concentration on porosity and conductivity.**

1.3 AGENDA OF RESEARCH

This section explains the theoretical design of the research. Firstly, within subsection 1.3.1, the objective of the research is explained. Finally, subsection 1.3.2, presents the research questions tackled within the current research.

1.3.1 Research Objective

The research objective of the research is

To investigate the influence of porosity of a-Si:H anode on battery performance by

- Varying PECVD deposition conditions to obtain intrinsic and n-type anode with variable porosities.
- Determining the porosity, optical and electrical properties of intrinsic and n-type anode.
- Evaluating the influence of varying dopant gas flow on porosity.
- Discharging the silicon-air battery by using porous a-Si:H anode.

1.3.2 Research Question

Within this subsection, the research questions to be answered within the current research is presented. The main research question is formulated based on the over¬arching research objective. A set of sub¬-research questions are constructed to answer the main research question.

Main RQ: What effect does porosity have on the discharge of the silicon-air battery?

Sub RQ-1 aims at understanding the variation in porosity and its properties by varying deposition conditions such as power and pressure. The evaluation consists of measuring the optical and electrical properties of various porosities.

- **Sub RQ-1:** What is the effect of PECVD deposition conditions on the material properties of intrinsic and doped silicon anode?

Sub RQ-2 intends to better understand the relationship between doping and porosity. This investigation is done by altering the doping concentration.

- **Sub RQ-2:** How does the variation in dopant gas flow change porosity and what is the effect on its optical and electrical properties?

1.4 OUTLINE OF THE RESEARCH

This section presents the overall narrative of the report. In all the required chapters, at the beginning of the chapter, a concise summary is provided. Similarly, at the end of the chapter, the relevant takeaways from the chapter is provided.

The motivation for deciding the components of the silicon-air battery for this research is described in Chapter 2. Within this chapter, the increase in specific discharge capacity by modifying the anode is discussed. The steps carried from the beginning till the end of the battery discharge have been explained in Chapter 3. The material deposition and material characterization techniques are also described.

The models used for determining the porosity and effective conductivity of a-Si:H film are provided in Chapter 4. The importance of percolation strength is described. Moreover, various Effective Medium Approximation (EMA) models are compared within this chapter. The results of the influence of deposition conditions on the deposition rate and material structure are provided in Chapter 5. Additionally, the characterization of the deposited material such as optical and electrical properties are analysed. The effect of doping on porosity is presented in this chapter.

The results of the discharge of silicon-air battery using a-Si:H is discussed in Chapter 6. Additionally, the problems faced during the experiment have also been described. The discharge curves of silicon-air battery using c-Si and a-Si:H as the anode are presented in this chapter.

This report ends with the conclusion for the research in Chapter 7. Within this chapter, the answer to all the sub-questions and research question have been answered. Finally, the recommendations arising from this research have been listed.

2 CELL DESIGN CONSIDERATIONS

2.1 INTRODUCTION

The main components of a battery are the anode, the cathode and the electrolyte. This chapter describes the type of anode, cathode and electrolyte used in this research and the motivation behind it. In order to decrease the effect of passivation, the overall dissolution rate of the discharged product must be higher than its generation rate. The overall dissolution rate can be improved by increasing the surface area of the anode and by constantly refreshing the electrolyte during discharge [19]. The surface area of silicon anode can be enhanced by several orders of magnitude by making it porous and by texturing. These techniques will be discussed in Sub-section 2.4.2.

2.2 ELECTROLYTE

A silicon-air battery can be discharged by using two types of electrolytes: RTIL and alkaline electrolyte. Cohn and Ein-Eli conducted a study using RTIL, which resulted in low corrosion rates [15] and Zhong et al. investigated the discharge of silicon-air battery using alkaline electrolyte to achieve high capacity silicon-air battery [74]. This section investigates the choice and the concentration of the electrolyte used.

2.2.1 Why KOH?

The use of EMI·(HF)2.3F ionic liquid-based electrolyte demonstrated an unlimited shelf life with a working potential in the range of 1.0–1.2 V and partially solved the issue of corrosion of the silicon anode [18][19]. But the practical applicability of such a battery system is complicated because of the presence of fluoride [48]. This causes severe safety issues and additional costs would be required for precaution. In addition, RTIL exhibits low ionic conductivity and high viscosity thus limiting the energy density [64].

On the other hand, the alkaline electrolyte comprises silicon, potassium, oxygen, and hydrogen elements that are compatible with the environment [74]. Another reason for employing alkaline electrolyte is its capability of dissolving $Si(OH)_4$ [18]. The passivating layer, SiO_2 is insoluble at low pH and has a high solubility in highly basic solutions that ensure further consumption of silicon [8].

In this study, the alkaline electrolyte used is KOH. The reason for this is

its high conductivity of 73.5 1 cm^2/equiv compared to the conductivity of NaOH and LiOH which is 50.11 1 cm^2/equiv and 38.7 1 cm^2/equiv respectively [35].

2.2.2 KOH Concentration

The OCV and discharge potential of the silicon-air battery are dependent on the concentration of the electrolyte. Zhong et al. suggested that a high concentration of KOH is used to achieve high OCV [74]. They observed the change in OCV as a function of KOH concentration. At concentrations of 6 M, 2 M, and 0.6 M the recorded OCV for 24 hours are 1.32 +/- 0.01 V, 1.23 V and 1.10 V respectively. This correlation between KOH concentration and OCV can be seen in Fig 2.1.

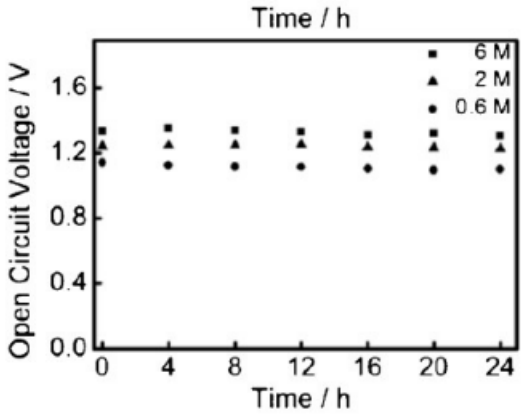

Figure 2.1: Open-Circuit Voltage for different concentrations of KOH. Higher KOH concentration leads to higher voltage. Image taken from [74].

Zhong et al. applied a discharge current of 0.05 mA/cm^2 [74]. The operating potentials obtained for this value of current density are 1.01 V, 1.06 V and 1.18 V for 6 M, 2 M and 0.6 M respectively.

However, a drawback of using high concentration of KOH is the corrosion

Table 2.1: Specific capacity for different concentrations of KOH. The corrosion effect is less for low KOH concentration and has high specific capacity. Table adapted from [74].

Current density	KOH concentration	Mass of silicon	Specific capacity
0.5 mA/cm^2	6 M	2.26 mg	154.8 mAh/g
0.5 mA/cm^2	2 M	1.63 mg	214.7 mAh/g
0.5 mA/cm^2	0.6 M	0.49 mg	715.7 mAh/g
1 mA/cm^2	0.6 M	0.58 mg	1206.0 mAh/g

effect of silicon anode [28][10][57]. As the concentration of KOH increases, the mass of silicon lost due to corrosion effect also increases. This corroding effect with the increase in KOH concentration and their specific capacities are tabulated in Table 2.1. These values distinguish the effect of corrosion

based on KOH concentration. The corrosion rates for KOH concentrations of 6 M, 2 M and 0.6 M are 1.34 m/h, 0.95 m/h and 0.24 m/h respectively. It is noticed that the corrosion is substantially reduced at a low concentration of KOH and has the highest specific capacity.

After Zhong et al., Durmus et al. also investigated the effect of KOH concentration on the discharge potential at low discharge current density [19]. At a KOH concentration of 6 M the conductivity of KOH electrolyte reaches a maximum and decreases with further increase of KOH concentration [27]. The increase in discharge potential with the KOH concentration is expected due to a change in activity and conductivity of the electrolyte [27][56]. However, according to Durmus et al., the change in conductivity of KOH should not result in the change of discharge potential by 100 mV at low current density.

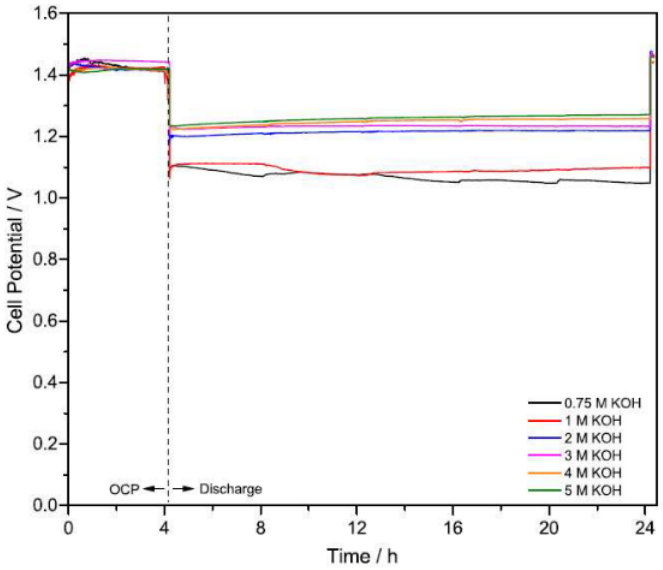

Figure 2.2: The OCV and discharge potential curves for different concentrations of KOH. Image taken from [19].

As seen from Fig 2.2, the discharge potential for low concentrations (up to 1 M) and high concentrations (2 M and above) are 1.1 V and 1.2 V respectively. For a high concentration of 5 M, the discharge potential increases slightly to 1.27 V. This suggests that the change in discharge potential is attributed to the surface reaction kinetics of silicon anode. These surface reactions cause low overpotentials and thus lead to a higher discharge potential.

2.3 CATHODE

The air electrode used in this experiment incorporates activated carbon powder pressed into a nickel mesh. The catalyst present for oxygen reduction reaction is manganese oxide. Such an air electrode is produced by Electric-Fuel.

According to Prins's study [51], pre-wetting of air electrode in KOH solution before the battery discharge exhibited an increase in discharge time and discharge potential. Pre-wetting increases the micro-pore area as other atmospheric gases besides oxygen might be suffocating the micro-pores of the air electrode. It also helps in adsorbing OH^- ions that contribute to the oxygen reduction reaction activity.

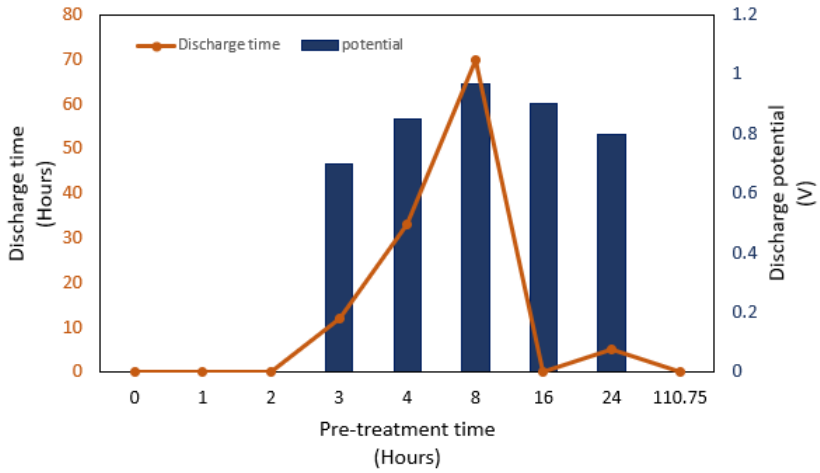

Figure 2.3: Discharge time and discharge potential for different hours of pre-wetting. Image adapted from [51].

The prewetting time of the air electrode was varied and the resulting discharge potential and discharge time is shown in Fig 2.3. A pre-wetting time of 8 hours displays the highest discharge potential and discharge time. A minimum of 3 hours of pre-wetting is required to notice an increase in these values and beyond 110.75 hours the discharge time and discharge potential showed a similar effect as that of no pre-wetting.

2.4 ANODE

As the name suggests, in a silicon-air battery silicon is the anode. Typically, the anode used is c-Si anode but the silicon anode requires to be modified to resolve the problems of corrosion and passivation to some extent. The main focus of this thesis is to reduce the passivation effect by increasing the surface area of the anode. This section discusses about the type of anode used in a silicon-air battery and reviews the effect of modification of silicon anode.

2.4.1 Types of anodes

Cohn and Ein-Eli conducted experiments to record corrosion current, corrosion rate, and polarization voltammograms for silicon anodes and air cathode. Fig 2.4 and Fig 2.5 represent the factors based on which the type of silicon is chosen. In the Fig 2.4, it is seen that the corrosion rates are lower for p-type silicon when compared to n-type silicon. This suggests the use of p-type silicon for battery discharge.

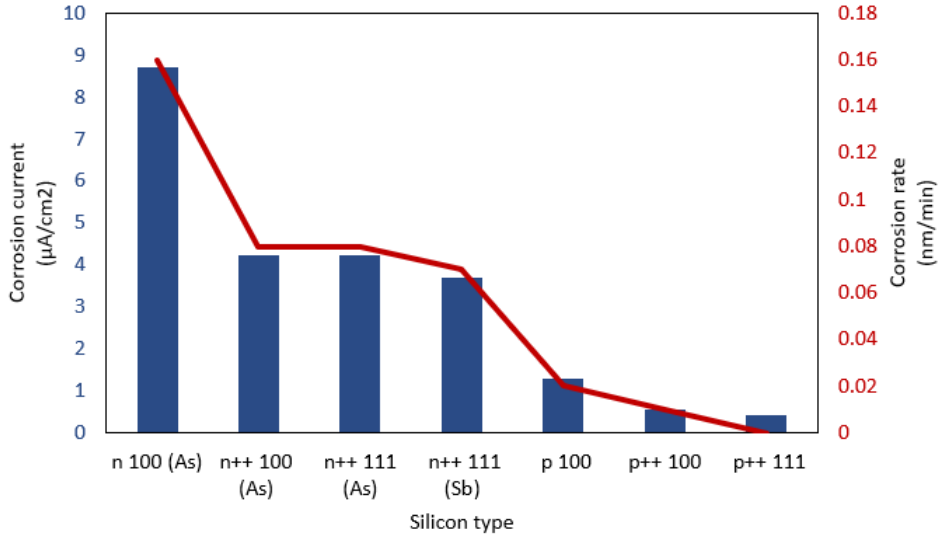

Figure 2.4: Corrosion current and corrosion rate for different levels of doped silicon. Low corrosion rate for highly doped silicon. Image adapted from [15].

According to Fig 2.5, at low current densities highly doped n-type silicon exhibits a wide potential gap with reference to the air electrode potential and at high current densities p-type silicon exhibits a wider potential gap. Since cell potential is the key aspect in optimizing the battery performance, the use of highly doped n-type silicon is recommended due to its wide potential gap at low current density.

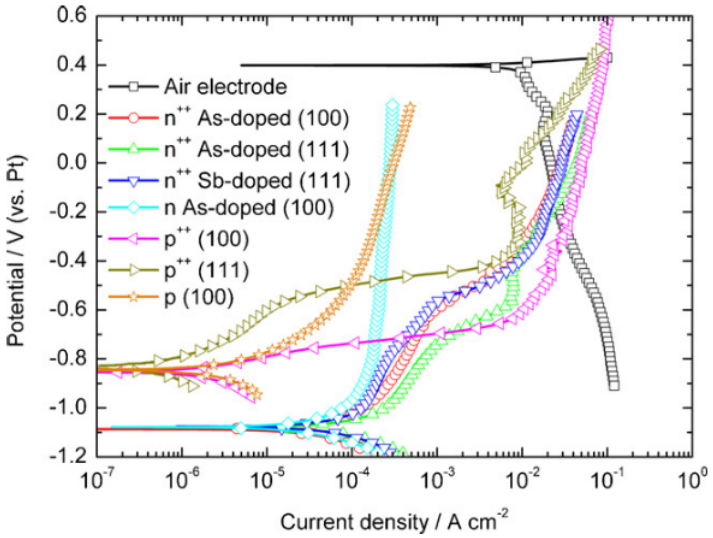

Figure 2.5: The potential of the different tested electrodes versus the platinum reference electrode at different current densities. The potential gap between n-type silicon and air electrode is bigger at low current densities. The potential gap between p-type silicon and air electrode is bigger at high current densities. Image taken from [15].

Zhong et al. also examined the influence of doping on the cell potential [74]. They concluded that the use of highly doped silicon is preffered as it displays a higher cell potential. This is attributed to the low internal resistance as the doping concentration is increased.

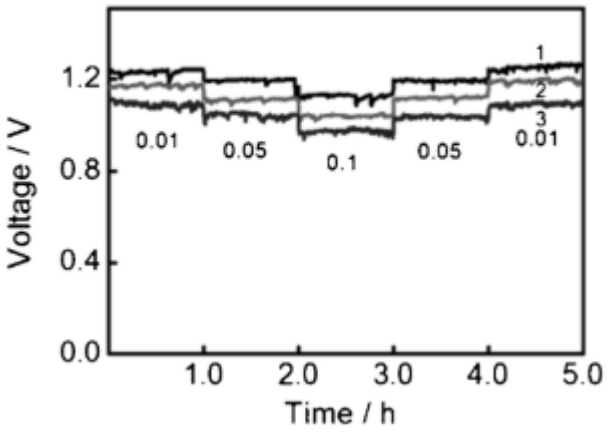

Figure 2.6: Voltage of different levels of doped silicon. Higher concentration exhibits high voltage. Image taken from [74].

2.4.2 Modification of silicon anode

The use of silicon anode in aqueous electrolyte gives rise to corrosion and passivation reactions. The passivation reaction leads to the formation of SiO_2 that deposits on the anode. However, as mentioned in Section **??**, the modification of silicon anode by increasing the surface area increases the

dissolution rate. As the surface area of silicon is increased more silicon is exposed to the electrolyte. This accelerates the dissolution of $Si(OH)_4$ in the electrolyte and unblocks the silicon anode for further consumption. Another way of increasing the surface area of silicon is by introducing pores into it. It allows the electrolyte to reach the areas of silicon that otherwise would not have been accessed by the electrolyte. The results of the battery performance based on the modified silicon anode have been mentioned below.

First, Zhong et al. textured the silicon anode by the metal-assisted electroless chemical etching technique [74]. The battery is discharged by applying a current density of 0.05 mA/cm^2 for both modified and unmodified anodes. The galvanostatic discharge curve for the unmodified anode shows a potential of 1.1 V with a discharge time of fewer than 10 minutes. Whereas for the modified (textured) anode, the galvanostatic discharge curve exhibits a potential of 1.2 V with a discharge time of over 30 hours. Here, the discharge curve is shown for 30 hours. The behavior of the discharge curve for both the anodes are shown in Fig 2.7.

The SEM images taken after the discharge of both modified and unmodified silicon anode are shown in Fig 2.8. The unmodified silicon anode exhibits a smooth surface that indicates the limitation of exposure of electrolyte to the silicon and the modified anode exhibits a porous structure that assists in the etching of SiO_2 from the anode surface and ensures continuous discharge.

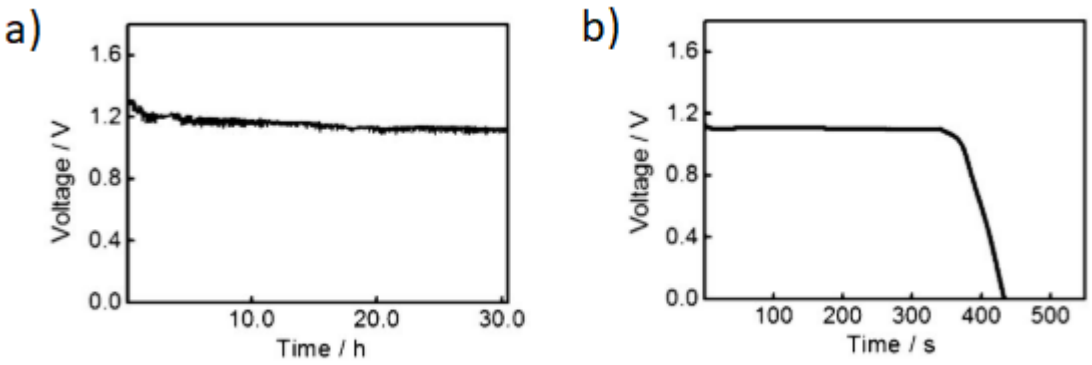

Figure 2.7: Comparison of battery discharge performance of (a) modified and (b) unmodified anode. The modified anode exhibits high voltage and long discharge time. Image taken from [74].

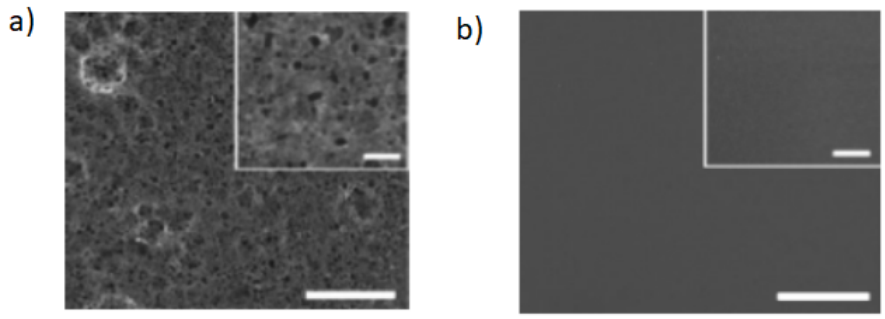

Figure 2.8: SEM image of (a) modified and (b) unmodified anode after discharge. Image taken from [74].

To avoid the restrictions caused by the rigid structure of the wafer-based silicon anode, Garamoun et al. employed amorphous silicon (a:Si:H) as the anode. The a:Si:H is deposited on Asahi glass by using the PECVD technique. The dissolution of a:Si:H is high in an alkaline electrolyte in contrast to the silicon wafer-based anode. The benefit of employing an a:Si:H anode is that it does not require any surface modification prior to the battery discharge. Although the wafer-based porous silicon anode exhibits a high discharge time, eventually the anode gets covered by SiO_2 and stops the battery discharge.

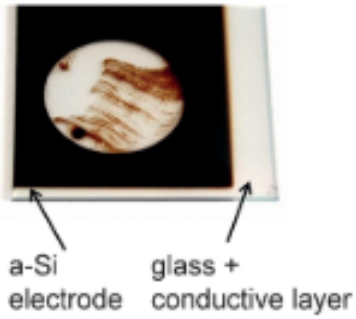

Figure 2.9: Complete dissolution of a:Si:H in alkaline electrolyte. Image taken from [25].

The discharge curves obtained by Garamoun et al. for a:Si:H and a-SiC anode types are shown in Fig 2.10 [25]. The battery discharge was performed by using a current density of 7.9 $\mu A/cm^2$ and 0.01 M KOH electrolyte. The specific capacity of a:Si:H and a-SiC reached a maximum of 219 mAh/g and 269 mAh/g. These experiments indicated only 5.5% consumption of silicon from a:Si:H anode which means most of the silicon is lost to corrosion reaction or because of self-discharge.

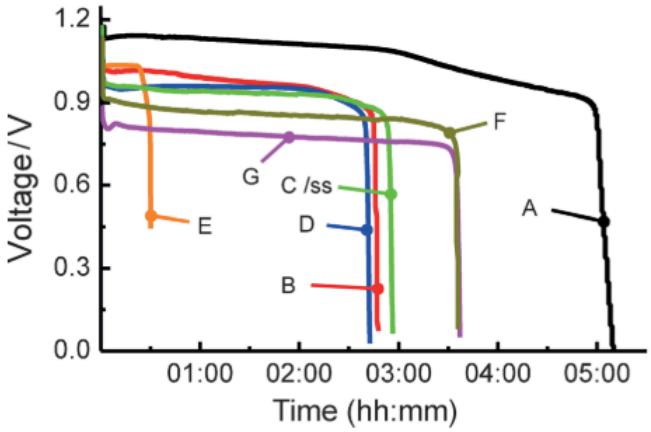

Figure 2.10: Discharge curves of different configurations of a:Si:H anode (A to E) and a-SiC anode (F to G). Curve C consisting of a:Si:H anode has the highest specific capacity. Image taken from [25].

Park et al. employed p-type nanoporous silicon as the anode. The pore thickness and pore size was controlled by varying the electrochemical etching time. Fig 2.11. verifies the increase in discharge potential and discharge time for nPSi when compared to flat Si. The applied current density is 5 $\mu A/cm^2$. The drop in voltage of flat Si points out the presence of passivation that blocks the silicon anode because for nPSi the specific capacity improved by 60 times that of flat Si.

Fig 2.12 presents the discharge curves for various nPSi thicknesses and pore sizes. The thicker pores and smaller diameters play a role in the increased discharge time and capacity. The drop in voltage for thicker pores and smaller diameter pores is not sudden and exhibits a more stable curve as the passivation effect is delayed. This is due to the increased surface area of the anode.

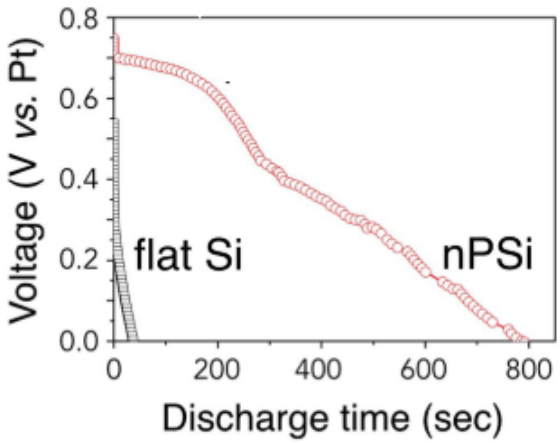

Figure 2.11: Comparison of voltage and discharge time of flat Si and nPSi silicon. nPSi has higher voltage and discharge time. Image taken from [48].

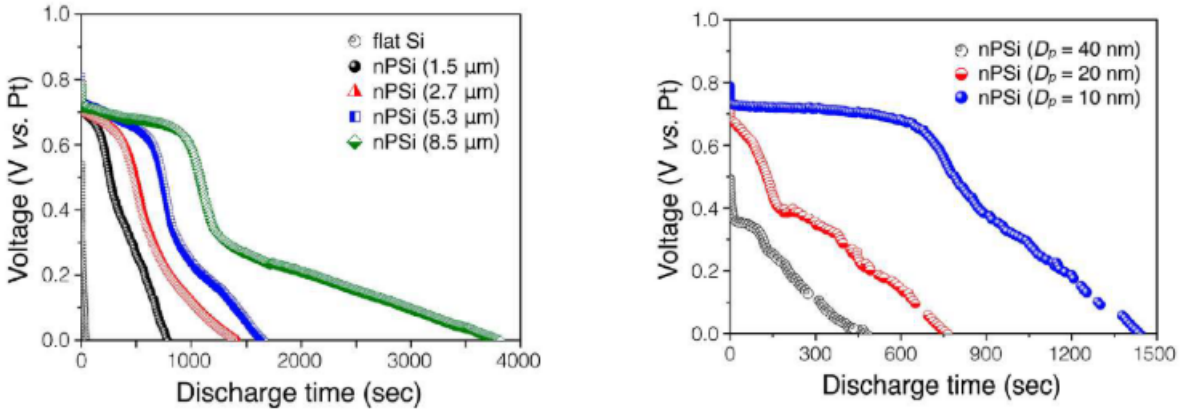

Figure 2.12: Discharge curves for different pore thickness (left) and pore diameter (right). Thick pores and thin diameters show high voltage and discharge time. Image taken from [48].

Park et al. discharged the nPSi in a battery at a current density of 1 µA/cm^2 and 10 µA/cm^2 [48]. As seen in Fig 2.13, the nPSi anode discharged at 1 µA/cm^2 operated longer than the anode discharged at 10 µA/cm^2. The discharge voltage was flat for 24000 seconds (1 µA/cm^2) and 600 seconds (10 µA/cm^2). This is because of the amplified surface passivation at high current densities. After the first discharge, the oxide layer was removed and the battery was discharged again. The new discharge curve exhibited an increase in the discharge time and the voltage was stable for 48000 seconds when compared to the battery discharge without the oxide removal step. This confirms the presence of an oxide layer after the initial discharge that prevents the battery from discharging any further.

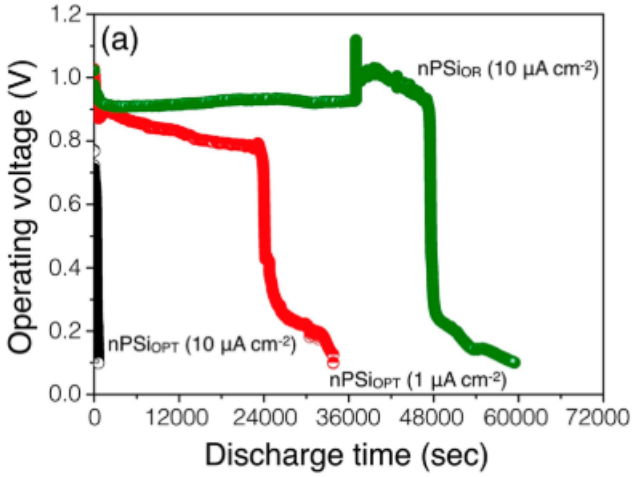

Figure 2.13: Discharge curves of a battery at different discharge current densities and after the oxide removal step. Low current density shows better performance and can be discharged further after removal of the oxide layer. Image taken from [48].

Apart from increasing the surface area of the anode to reduce the effect of passivation, the appropriate balance of electrolyte supply can also ensure continuous dissolution of Si(OH)4. The assembly of such battery is shown in Fig 2.14

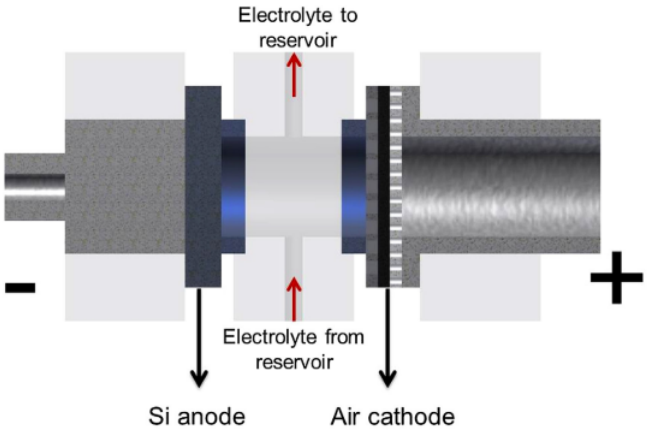

Figure 2.14: Illustration of silicon-air battery with a scope of refreshing the electrolyte. Image taken from [19].

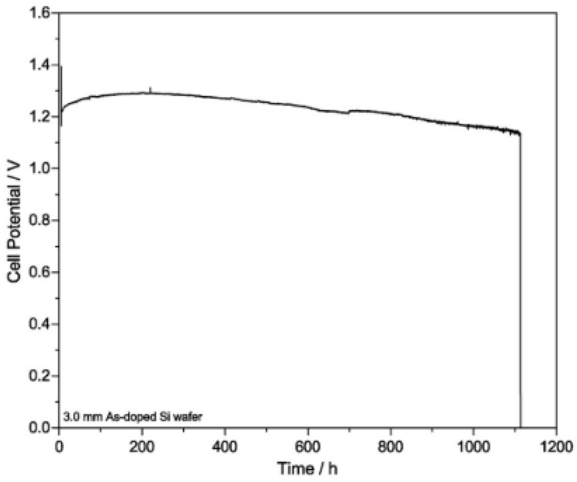

Figure 2.15: Discharge curve of the battery until complete consumption of silicon while continuously refreshing the electrolyte. The discharge lasted for 1100 hours. Image taken from [19].

Here, an n-type unmodified silicon wafer of thickness 3 mm is used as an anode. The battery performance of such an anode is seen in Fig 2.15. The discharge potential and discharge time of this battery are 1.2 V and 1100 hours respectively. The reason for the end of discharge is the complete consumption of silicon, which otherwise would be limited by the passivation

layer. This proves that the battery performance can be increased by continuously refreshing the electrolyte. The reaction product formed is washed away as a fresh batch of electrolyte is used.

2.5 CONCLUSION FOR BACKGROUND ON SI-AIR BATTERY

During the discharge process of a silicon-air battery, silicon is oxidized at the anode side and oxygen is reduced at the cathode side. As a result, silicic acid ($Si(OH)_4$) is formed as the discharge product. In addition to the discharge reaction, corrosion and passivation reaction also occur. During corrosion, the battery goes through a self-discharge process. Corrosion also causes hydrogen evolution when the electrons move towards the anode instead of moving towards the cathode through the external circuit. Passivation occurs when the dissolution rate of the discharge product is slower than the generation rate. This forms SiO_2 to attach on silicon anode thus, stopping the battery from discharging.

The components in a silicon-air battery are anode, cathode and electrolyte. Although the performance of silicon-air battery is greater in RTIL, KOH is used because of safety issues with RTIL. The anode is modified by increasing its surface area to enhance the specific discharge capacity. This is achieved by varying the porosity of the anode. The type of anode employed in this research is a-Si:H and the cathode is powdered carbon pressed in to a nickel mesh.

3 EXPERIMENTAL METHODS

3.1 INTRODUCTION

The process for obtaining porous silicon anode is described in this chapter. It entails depositing porous a-Si:H and determining its characteristics using material deposition and characterization procedures. To attain a large discharge capacity, the silicon anode must be changed, as indicated in Subsection 2.4.2. The procedure used to create porous silicon anode is depicted in Fig 3.1.

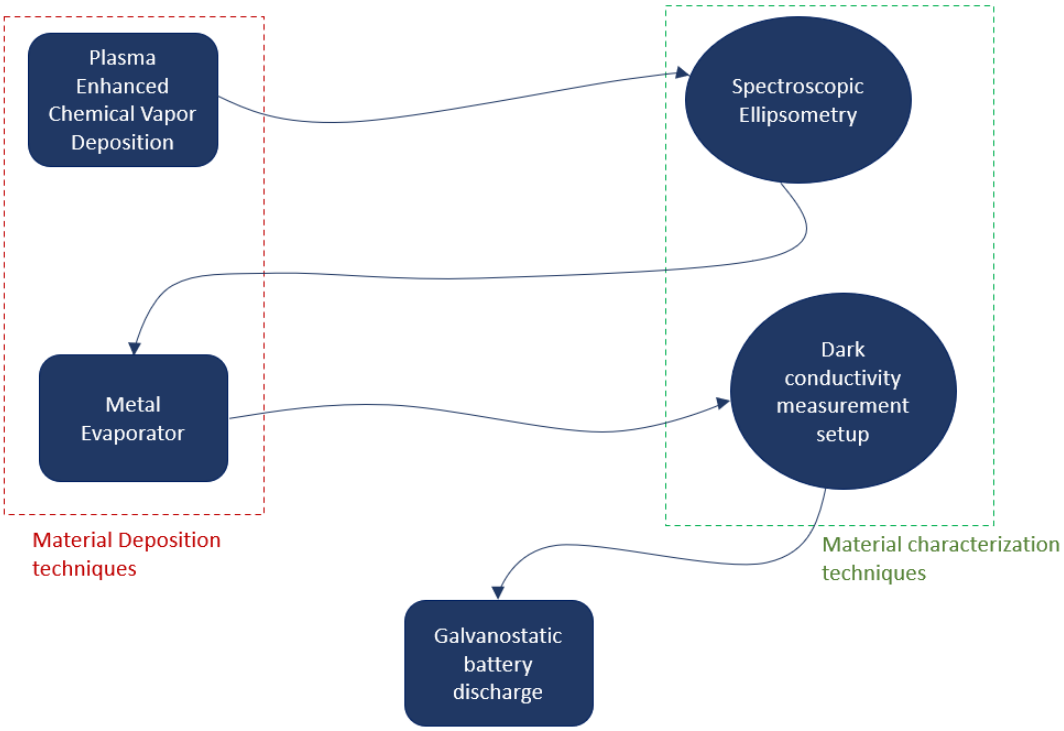

Figure 3.1: The process from forming the silicon anode to discharging the Si-air battery in chronological order.

From the deposition of the silicon anode through the discharge of the battery, the following steps are followed:

1. A thin layer (nm) of porous a-Si:H was deposited on Corning glass substrate using PECVD technique.

2. Spectroscopic ellipsometry was used to evaluate the optical constants of this porous a-Si:H layer.

3. A metal evaporator was used to deposit Al onto the porous a-Si:H layer.
4. The electrical conductivity of the deposited porous a-Si:H was determined using a dark conductivity testing setup.
5. Battery discharge experiments were conducted using c-Si and a-Si:H anode.

3.2 MATERIAL DEPOSITION TECHNIQUES

This section addresses the material deposition techniques used for the work presented in this thesis. The preparation of a-Si:H anode using PECVD technique and the deposition strategy for obtaining films of various porosities is described in Sub-section 3.2.1. This section also includes the types of substrates that were used and the treatment that was required prior to deposition in Sub-section 3.2.2. The principle and application of metal evaporator is discussed in Sub-section 3.2.3.

3.2.1 PECVD

PECVD is a chemical vapor deposition process in which gaseous species react on solid substrates to form solid films. In this technique the energy used to activate the chemical reactions originates from a plasma that is created by Radio Frequency (RF) discharge between two electrodes. Hence, the films can be deposited on substrates at low temperature (< 300 °C) compared to Chemical Vapor Deposition (CVD) (> 300 °C) [46].

For the deposition of a-Si:H on different substrates the PECVD machine AMOR was used. The AMOR has four deposition chambers, with each chamber having a set of precursor gases. The samples were deposited in deposition chamber 4. a-Si:H was deposited using 13.56 MHz RF mode. The distance between the two electrodes was 21 mm and the substrate temperature was maintained constant at 290 °C. This temperature was chosen because the conductivity of the film is higher around 280 °C [9]. a-Si:H depositions are achieved by introducing reactant gases between parallel electrodes: a grounded electrode and an RF-energized power electrode. The flow of pressure is controlled by a butterfly valve. This is seen in Fig 3.2.

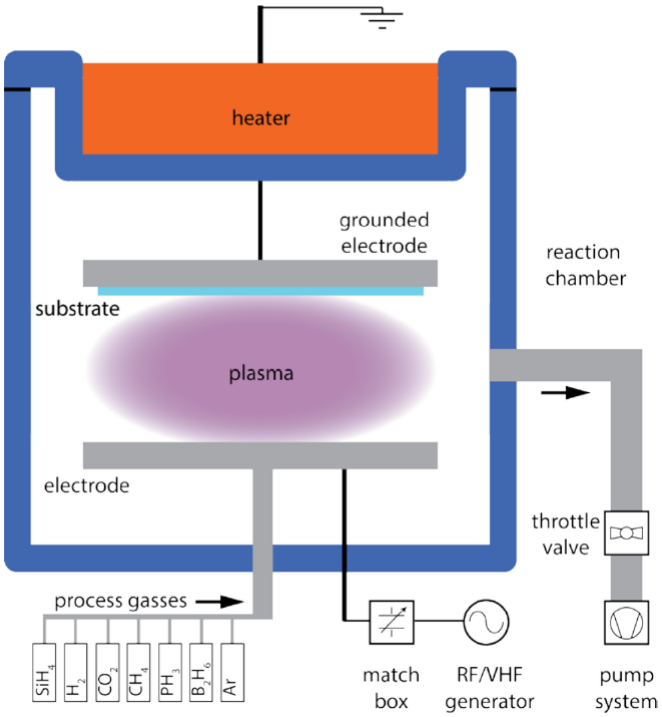

Figure 3.2: Illustration of Plasma Enhanced Chemical Vapor Deposition [60]. The substrate is placed on the grounded electrode (top). There is an inlet on the left for the source gases and an outlet on the right for exhaust gases. Image adapted from [72].

Deposition strategy

The structural and optical properties of the film can be controlled by varying parameters like RF power, deposition pressure, temperature, gas flow rate, and electrode distance. The focus of this research was to vary the porosity of the film by varying parameters like deposition pressure, deposition power, and dopant flow rate.

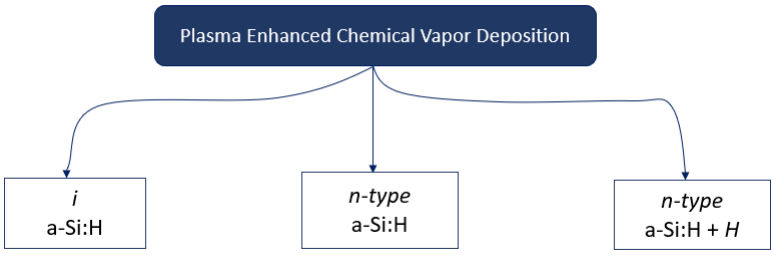

Figure 3.3: Types of anodes deposited by PECVD.

First, an intrinsic a-Si:H film was deposited by varying the deposition pressure and deposition power. SiH_4 (silane) was used as a precursor to deposit undoped a-Si:H. The gas flow rate of SiH_4 was constant. The depositions

were conducted by varying the deposition pressure from 0.9 mbar to 1.4 mbar and varying the deposition power from 5 W to 15 W.

Several studies defined the relationship between the varying parameters (pressure and power) and the deposition rate. Deposition at a high power gives rise to high rate of gas dissociation, which leads to an increase in deposition rate [37]. Additionally, the deposition at high pressure also leads to an increase in the deposition rate as a result of increased collision between the gas molecules. This reduces the path between the reactant molecules. But, as the pressure increases further, the reaction with the substrate decreases which leads to a decrease in deposition rate [38].

Since undoped a-Si:H exhibited low conductivity, a-Si:H was doped to increase the conductivity. A gaseous mixture of SiH_4 and PH_3 diluted in 2% H_2 was used to deposit n-type a-Si:H. A series of depositions was conducted by varying deposition pressure and deposition power from 0.7 mbar to 1.4 mbar and varying the deposition power from 5 W to 20 W, respectively. The gas flow rate of SiH_4 and PH_3 was constant at 40 sccm and 11 sccm, respectively. The deposition conditions for undoped and doped a-Si:H layer are mentioned in Table 3.1.

Table 3.1: Deposition conditions for undoped and doped a-Si:H thin films.

Deposition conditions	Values
Reactive precursors	SiH_4 (undoped) + PH_3 (doped)
RF Power	5-20 W
Deposition pressure	0.7-1.4 mbar
Deposition temperature	290°C
F(SiH_4)	40 sccm
F(PH_3)	11 sccm

The undoped a-Si:H layer was deposited by using the precursor SiH_4 and the doped n-type a-Si:H layer was deposited by using the precursors PH_3 and SiH_4. The gas flow rate of all the precursors was kept constant. Since doping has an effect on porosity, this thesis also focuses on the effect of dopant gas flow on porosity. This was achieved by employing the precursors SiH_4, PH_3, and H_2. The gas flow rate of PH_3 and H_2 was varied but the total gas flow rate of both the gases was kept constant to match the gas flow rate of PH_3 from previous depositions. By matching the gas flow rate, the residence time of all the gases in plasma remains the same.

3.2.2 Substrate for deposition

The a-Si:H films were deposited on Corning glass and Asahi glass. Corning glass was used for material characterization whereas Asahi glass were used in the battery assembly as anode. After the measurement of the deposited layer on Corning glass the a-Si:H layer was deposited on Asahi glass. The a-Si:H layer deposited on various substrates is shown in Fig 3.4 and their dimensions are listed in Table 3.2.

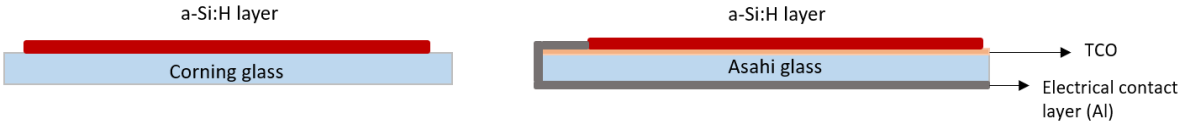

Figure 3.4: a-Si:H layer on Corning glass (left) and Asahi glass (right).

Table 3.2: Types of substrates.

Substrate	Dimension (cm)	Thickness (mm)
Corning glass	10 × 10	0.7
Asahi glass	10 × 2	1.5

Corning glass substrates were first cleaned for 10 minutes in two ultrasonic baths consisting of acetone and isopropyl alcohol. The cleaned substrates were then etched in hydrofluoric acid (HF) for 270 seconds followed by immersing in De-ionized (DI) water and finally drying in a nitrogen stream [4]. Etching was done to improve adhesion between the film and the substrate by increasing the roughness of it [12]. As the KOH electrolyte in the silicon-air battery etches the a-Si:H layer, Asahi glass (glass covered by fluorinated tin oxide, SnO_x:F) was used as the substrate. Asahi consists of a Transparent Conductive Oxide (TCO) that serves as a textured surface exhibiting improved adhesion of a-Si:H film [25]. The Asahi glass was also immersed in an ultrasonic bath consisting of acetone and isopropyl alcohol for 10 minutes, respectively.

3.2.3 Metal Evaporator

The metal evaporator is used to deposit metallic layers like Al and Silver (Ag). Here, the metal evaporator was used to deposit Al layer to form an electrical contact on the substrates (Corning glass and Asahi glass). Metal evaporation is a Physical Vapor Deposition (PVD) technique that comprises two main techniques: resistive evaporation, and electron-beam evaporation.

Irrespective of the technique, the metal evaporator heats the metal to be deposited above its melting point. This heated metal then condenses on the cooler surface of the substrate.

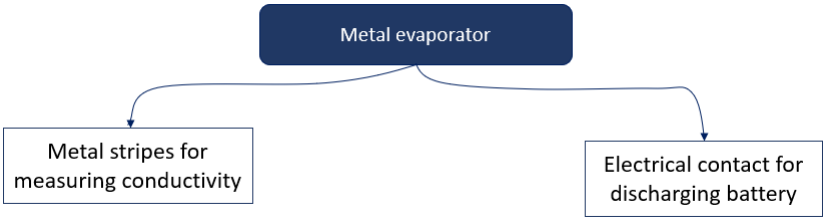

Figure 3.5: Metal evaporator is used for depositing Al for measuring conductivity and serving as an electrical contact to the anode.

In this research, electron-beam evaporation was employed. For electron-beam evaporation, the metallic source is loaded in a water-cooled crucible and is irradiated by an intense electron beam, which heats the source. The electron beam is emitted by a tungsten filament and directed by strong magnetic fields. For both resistive and electron beam evaporation, the metallic source evaporates and its atoms follow straight trajectories targeting the substrate.

In this work, the metal evaporator Provac Pro500S was used to deposit a layer of Al of 300 nm thickness on the n-type a-Si:H film. Provac Pro500S was also used to deposit an Al layer of 500 nm thickness on the front and backside of Asahi glass to bridge the electrical contact between the front and back sides.

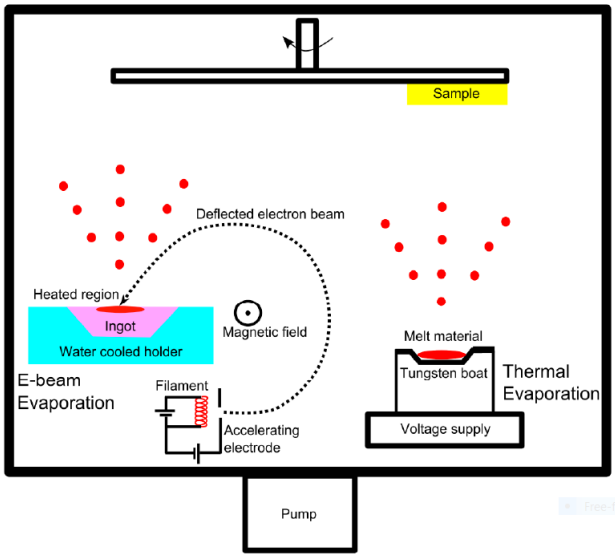

Figure 3.6: Schematic of metal evaporator used to deposit Al. Image adapted from [60].

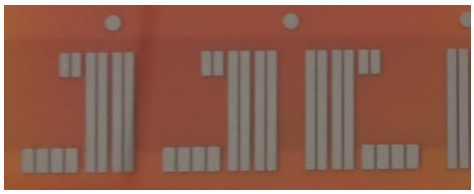

Figure 3.7: Al stripes deposited act as metal electrodes for measuring electrical conductivity.

3.3 MATERIAL CHARACTERIZATION TECHNIQUES

This section goes through how to measure the optical and electrical properties of deposited a-Si:H layers. Sub-section 3.3.1 describes the principle of spectroscopic ellipsometry and how it can be used to determine optical constants. In Sub-section 3.3.2, the dark conductivity setup used to assess the conductivity of the deposited layer is described.

3.3.1 Spectroscopic Ellipsometry

Ellipsometry measures the change in light polarization of the incident beam prompted by the reflection of the a-Si:H sample [70]. Ellipsometry is an optical measurement technique used to characterize optical constants i.e., n and k, the thickness of the film, and bandgap. These results are obtained by fitting an optical model.

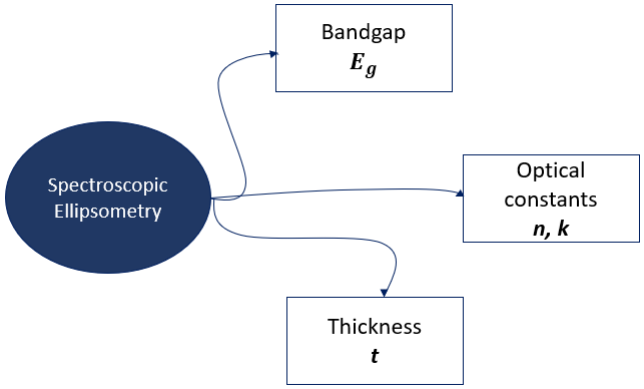

Figure 3.8: Spectroscopic ellipsometry is used to determine bandgap, optical constants and thickness of the layer.

Polarized light is used to characterize the optical properties of materials [22]. The measurement was carried out at different angles of incidence of 55°, 60°, 65°, and 70°. The substrate used for this type of characterization is Corning glass. Since glass is transparent, the backside reflections was avoided by applying tape to the backside. Because of the reflection and transmission caused by the substrate, parallel and perpendicular polarized light is obtained where s- polarization is perpendicular to the incident plane and p- polarization is parallel. The optical constants obtained are dependent

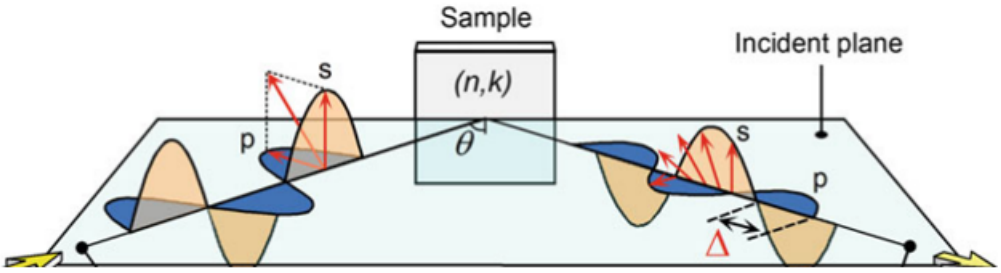

Figure 3.9: Illustration of the basic principle of SE. p- and s- polarizations are indicated by s and p [23].

on the amplitude and phase of p- and s- polarized light [23]. Ellipsometry measures the amplitude ratio (ψ) and phase difference (Δ) between p- and s- polarization. Fresnel equations were used to provide the magnitude of reflected fields in p- and s-polarized light.

$$\tilde{r_p} = \frac{\tilde{E}_r}{\tilde{E}_i} = \frac{n_t \cos\theta_i - n_i \cos\theta_t}{n_i \cos\theta_t + n_t \cos\theta_i} \tag{3.1}$$

$$\tilde{r_s} = \frac{\tilde{E}_r}{\tilde{E}_i} = \frac{n_i \cos\theta_i - n_t \cos\theta_t}{n_i \cos\theta_i + n_t \cos\theta_t} \tag{3.2}$$

$\tilde{r_p}$ and $\tilde{r_s}$ are Fresnel reflection coefficients for p and s polarized light.

Since ellipsometry directly measures the Psi (ψ) and Delta (Δ) parameters, the change in polarization is given by [22], where, ρ represents the change in polarization.

$$\tan(\psi)e^{i\Delta} = \rho \tag{3.3}$$

The Spectroscopic Ellipsometry used for characterization was J. A Woollam M2000DI. It covers a wavelength range of 193-1690 nm, with a data acquisition rate of 0.05 seconds and, the maximum thickness measured is 18 mm [65].

Since SE measures only the ellipsometric parameters (ψ) and (Δ) versus wavelength [70], the SE data must be analyzed by an optical model. The optical model incorporated for measuring the required values on a-Si:H layer is Cody-Lorentz [21]. CompleteEase software was used to analyze spectroscopic ellipsometry measurements and acquire material properties like optical constants (n,k), and the thickness of the film.

The optical model (Cody-Lorentz) used must overlap the measured data to have a good fit. The software compares the results of the model that is implemented in the software to the measured data. Based on differences between the calculated and measured optical parameters, the parameters of the model are adjusted and the optical parameters are recalculated. As seen

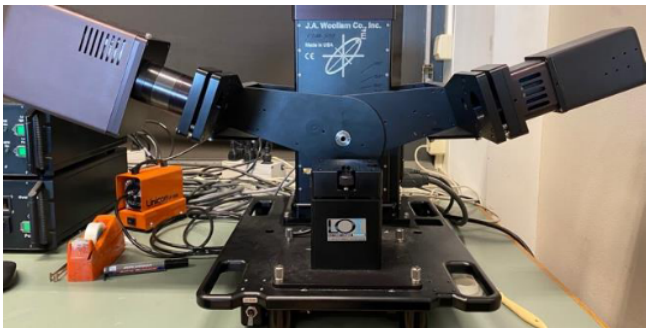

Figure 3.10: Spectroscopic Ellipsometry, J. A Woollam M2000DI.

from Fig.3.12, the black dotted line which represents the optical model overlaps the measured data indicating a good fit. The Mean Square Error (MSE) value is 17.7 which means it is a good fit for a thickness of 235 nm. The optical constants i.e., refractive index (3.69) and extinction coefficient (0.03965), and bandgap (1.69 eV) of the film were also acquired from the fit.

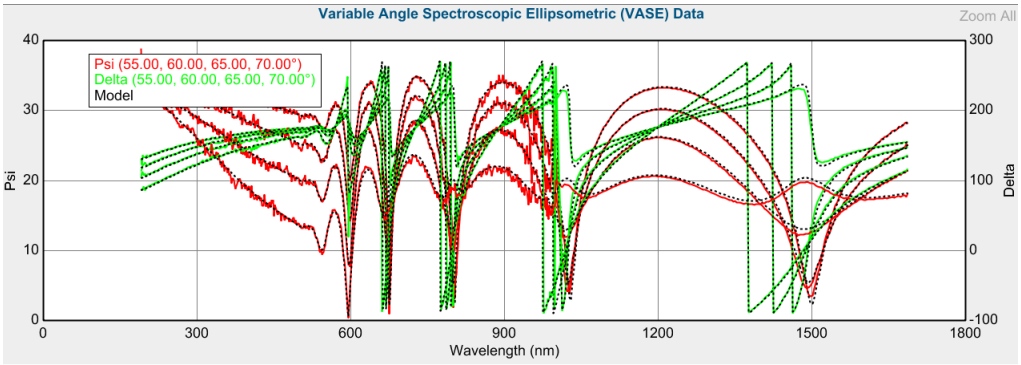

Figure 3.11: Model used to fit SE data. The black dotted line represents the model parameters and the colored lines represent SE data.

Fit Results

MSE = 17.720
Roughness = 3.50 ± 0.031 nm
Thickness # 1 = 235.24 ± 0.150 nm
Amp1 = 89.014 ± 1.6964
Br1 = 2.666 ± 0.0158
Eo1 = 3.813 ± 0.0165
Eg1 = 1.696 ± 0.004040
Ep1 = 1.701 ± 0.0406
n of a-Si parameterized @ 632.8 nm = 3.69402
k of a-Si parameterized @ 632.8 nm = 0.03965

Optical Model

Roughness = 3.50 nm (fit)
+ Layer # 1 = a-Si parameterized Thickness # 1 = 235.24 nm (fit)
+ Substrate = 7059_Cauchy

Figure 3.12: The optical properties and thickness of the film measured by SE where, n= refractive index, k= extinction coefficient, Eg1= Band gap.

3.3.2 Dark conductivity measurement setup

Dark conductivity measurement setup was used to measure the electrical conductivity of deposited a-Si:H films. This setup also measures the activation energy E_a, which is the energy difference between the Fermi level, E_F, and the bottom of the conduction band, E_C.

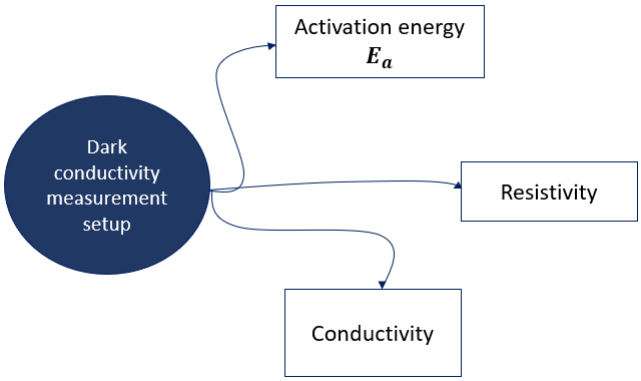

Figure 3.13: Dark measurement setup is employed to measure activation energy, resistivity and conductivity.

The relationship between the conductivity and activation energy is determined by the equation mentioned below:

$$\sigma = \sigma_0 \exp\left(E_a/kT\right) \tag{3.4}$$

To serve as a metal contact electrode, Al metallic stripes were deposited on the a-Si:H films as described in Sub-section 3.2.3. Two probe contacts were held in contact with the Al strips to measure conductivity. The conductivity of the film was calculated based on Ohm's law and geometrical parameters of the film and the metal stripes [50]. Equation 3.5 depicts the link between these parameters. With the help of these contacts, a potential was applied across the film and a current passes through the surface of the film as a result of this applied potential, which was measured by the dark conductivity measuring setup.

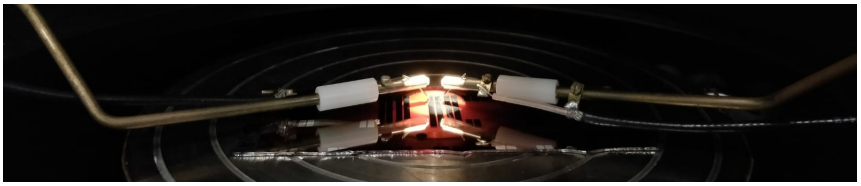

Figure 3.14: Contact of probes with Al to measure the electrical conductivity.

$$\sigma = \frac{I}{V}\frac{l}{wt} \tag{3.5}$$

where,
l is length of the metal electrode
w is width of the metal electrode
t is thickness of the film

The dark conductivity measurement setup used in this work was Keithley 6517B Electrometer/High Resistance Meter. For measuring the electrical conductivity as a function of temperature, the temperature between two coplanar electrodes was varied from 60 °C to 130 °C degrees with an interval of 5 °C. From the measurements, the dark measurement setup directly displays the resistance of the film as shown in Fig 3.16, from which the conductivity can be derived. The conductivity at room temperature was obtained by extrapolation.

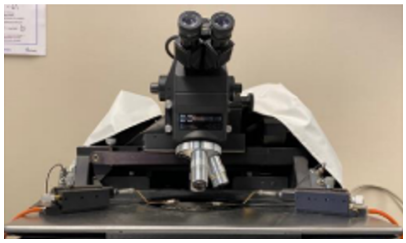

Figure 3.15: Microscope used to connect the probe to coplanar metal stripes.

Figure 3.16: Keithley 6517B Electrometer/High Resistance Meter displaying the resistance.

3.4 BATTERY DISCHARGE EXPERIMENTS

The main topic of interest in this research was to understand the performance of the battery by using porous a-Si:H anode. To compare the discharge capacity of this porous silicon anode with the discharge capacity of unmodified (pure 1 cm^2 silicon anode), first, discharge experiments were conducted using unmodified anode. In this experiment, p-type c-Si wafer was used as the unmodified anode.

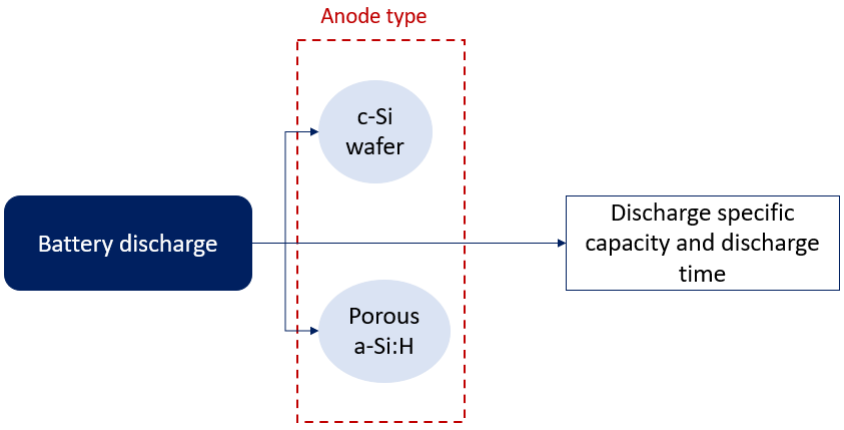

Figure 3.17: Types of anodes used to compare discharge specific capacity.

3.4.1 Cell Design

The battery cell consists of three parts, out of which two parts are identical. The electrodes are mounted on the outer two identical parts and the electrolyte is filled in the middle part. The middle part of the battery has an opening at the top to pour the electrolyte in. For the electrochemical reaction to take place, the anode and cathode must be in contact with the electrolyte and the metal spring must be in contact with the electrodes. For this reason, all three parts of the cell have an opening at the center for the components to be in contact. The area of the opening is 1 cm^2. The opening on the part on which electrical contact is made with the cathode functions as the oxygen inlet for the air cathode [51].

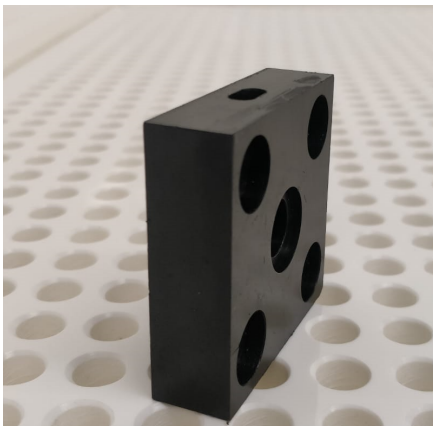

Figure 3.18: Electrode part of the battery cell assembly. The opening at the centre is 1 cm^2 where the electrode is placed.

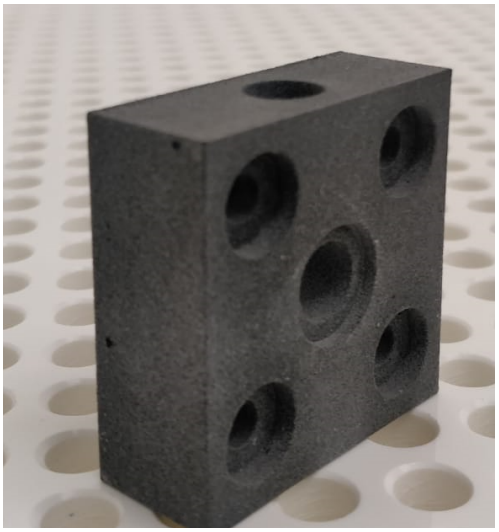

Figure 3.19: Electrolyte part of the battery cell assembly. The opening at the top is for pouring the electrolyte.

The three parts of the cell were assembled by placing the anode and cath-

ode on the opening and mounting it as shown in fig 3.20 . The electrolyte was poured after the cell was assembled. To avoid leakage, PTFE O-rings were placed around the opening of each part.

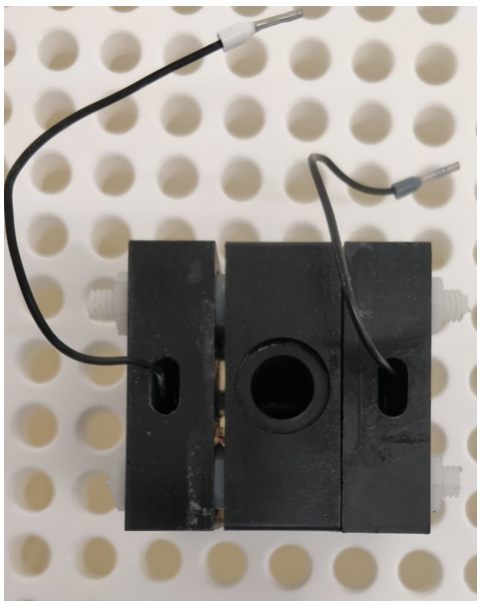

Figure 3.20: Top view of the battery cell assembly. The anode is placed on the left side, electrolyte is poured in the middle and the cathode is place on the right side.

3.4.2 Anode

As mentioned, first, p-type c-Si wafer was used as an unmodified silicon anode to study the performance of the battery during discharge. The performance of the battery was improved by using a current collector at the backside of the silicon anode. This current collector layer of 475 nm thickness was deposited by sputtering Al containing 1% silicon.

The typical size of the silicon wafer is 10 inches but the area of the silicon anode required for the discharge experiment is 1 cm^2. A laser cutter was used to cut the silicon wafer into small pieces. The laser was scribed into square shapes of 2 cm $\times$ 2 cm. After etching, the pieces can be separated manually. A larger size of the anode can be placed in the cell since the size of the opening ensures only 1 cm^2 is exposed to the electrolyte.

Finally, the modified silicon anode was used to investigate the effect of porous silicon on the performance of the battery during discharge. The n-type a-Si:H film deposited on stainless steel and Asahi glass as mentioned in Section 3.2.1 was used as the modified silicon anode. The stainless steel was cut into small pieces by using a manual cutter. Since the stainless steel is conductive, there was no need for the current collector. Asahi glass was cut into small pieces by using a glass cutter.

3.4.3 Cathode

The air electrode used in this research was provided by ElectricFuel. The air electrode comprises of porous carbon structure with manganese dioxide catalyst pressed into a nickel mesh [25].

Prins's [51] work suggested pre-wetting of the air cathode in the electrolyte solution to get an increased discharge specific capacity. The cathode was pre-wetted in the electrolyte solution for 4 hours prior to battery assembly.

3.4.4 Electrolyte

The electrolyte used in this research consists of a 0% KOH solution. This value was decided after discharging the battery with different concentrations of KOH solution. The solution was prepared by weighing 30 grams of KOH pellets and mixing them with water to form a 30% KOH solution.

3.4.5 Battery discharge

Galvanostatic discharge experiments were carried out using Autolab which is a galvanostat linked to Metrohm NOVA software. First, a discharge current density of 150 $\mu A/cm^2$ was applied then the dishcarge current density was lowered to evaluate the output potential of the cell. Initially, in each experiment, the battery was discharged after the battery was kept at OCV for 1 hour (60 minutes). During the OCV period, bubble formation could be noticed in the electrolyte. When the battery was discharged after an hour the voltage dropped below zero. This could be interpreted as the anode oxidation in the presence of KOH electrolyte. Therefore, the OCV time used to discharge was 15 minutes. After OCV time, the battery was discharged and the cell potential was recorded for every second. The battery discharge experiments were carried out with both c-Si wafer as anode and n-type a-Si:H porous anode.

3.5 CONCLUSION FOR EXPERIMENTAL METHODS

The deposition technique employed for the deposition of a-Si:H layer is PECVD. The optical properties of the deposited layer was modified by varying the deposition power and deposition pressure. Suitable precursors were used to obtain undoped and doped a-Si:H. Moreover, several depositions were also made by varying the dopant concentration. All the a-Si:H depositions were deposited on Corning glass, stainless steel, and Asahi glass. Depositions on Corning glass were used for material characterization and depositions on stainless steel and Asahi glass were used as anode for the discharge of silicon-air battery. After the deposition of a-Si:H layer, a metal evaporator was used to deposit Al stripes for measuring the conductivity of the deposited layer. Al was also deposited on the front and back side of Asahi glass to serve as an conductive layer for the battery discharge experi-

ments.

The optical properties like refractive index (n), extinction coeffecient (k) were obtained by using spectroscopic ellipsometry. The data acquired from SE was analyzed by the optical model Cody-Lorentz. The conductivity of the deposited a-Si:H layer was measured using the dark conductivity setup. The Al metallic stripes behave as metal electrodes that come in contact with probes for the measurement of conductivity.

The deposited a-Si:H layer and c-Si wafer were used as anode for the discharge of silicon-air battery. The silicon-air battery setup was designed to allow contact between the anode, cathode, and electrolyte. The cathode used in this discharge experiment is porous carbon and the electrolyte used is KOH. The silicon-air battery was discharged by using a galvanostat, Autolab. The discharge current density of the battery was 150 $\mu A/cm^2$ which was followed by lowering the discharge current density. The silicon-air battery was kept in open-circuit condition for 15 minutes.

4 MODELS FOR POROUS A-SI:H

4.1 INTRODUCTION

The porous a-Si:H structure is not the same as the c-Si structure. As a result, the porosity and conductivity of the deposited layers was evaluated by Bruggeman's effective medium approach model and percolation model. This chapter lists the different types of models available for calculating porosity and mentions the use of the percolation model for estimating the effective conductivity of the material.

4.2 POROSITY DETERMINATION

As multiple depositions were conducted by varying the deposition parameters, the structure and optical properties of each deposited layer would be different. Hence, the porosity of each deposited porous a-Si:H layer must be determined.

4.2.1 Porous silicon as an effective medium

Porous silicon is a heterogeneous material that consists of pores (voids) and silicon. Hence, the effective refractive index of porous silicon lies in between the refractive index of air and crystalline silicon (c-Si) (bulk silicon) [20]. The refractive index of a material can be used as a measure of density. A high refractive index represents a dense structure and a low refractive index represents a porous structure. The silicon in the deposited porous a-Si:H layer exhibits absorption of light up to a wavelength of about 700 nm and the pores do not absorb light because they are transparent [39]. The refractive index and extinction coefficient obtained from spectroscopic ellipsometry are shown in Fig 4.1.

In an effective medium, the two phases, i.e. pores and silicon, are averaged as one phase instead of differentiating silicon as host and the voids as inclusion in the host [53], [45], [42]. As both the pores and silicon do not absorb light in the IR region, the porous silicon is considered as an effective medium. As a result, the refractive index of porous silicon is determined in the IR region [8]. Moreover, the pore size ($\sim$ 10 nm) in porous silicon is much smaller than the wavelength of light in the IR region ($>$ 800 nm) [39]. Effective medium approach evaluates the effective refractive index of porous silicon.

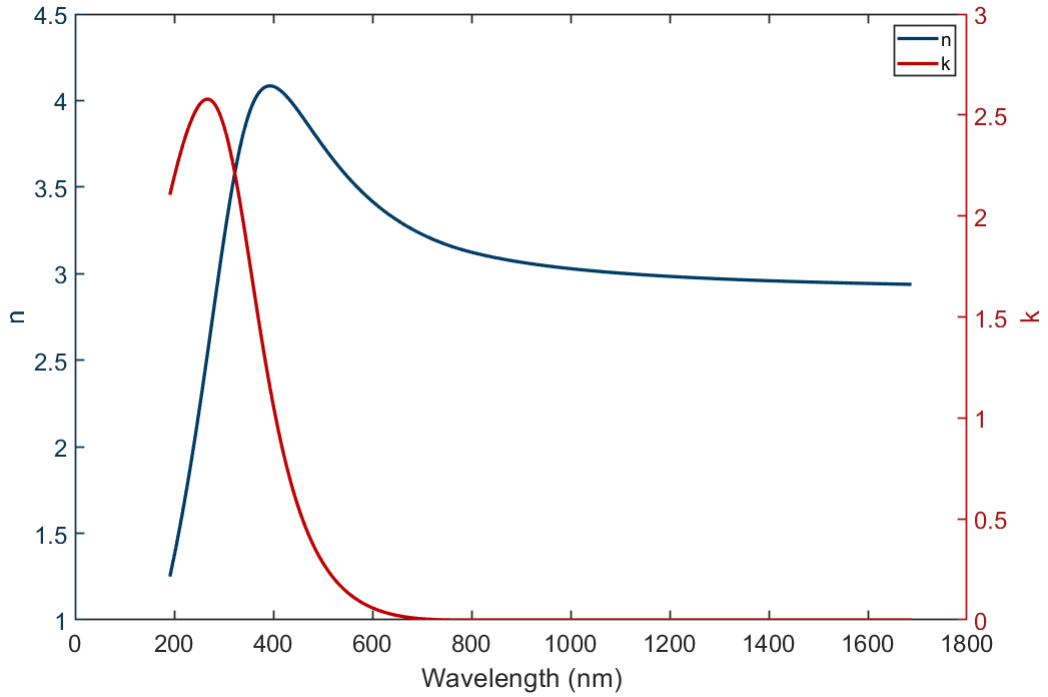

Figure 4.1: Refractive index and extinction coefficient of a-Si:H layer acquired from spectroscopic ellipsometry.

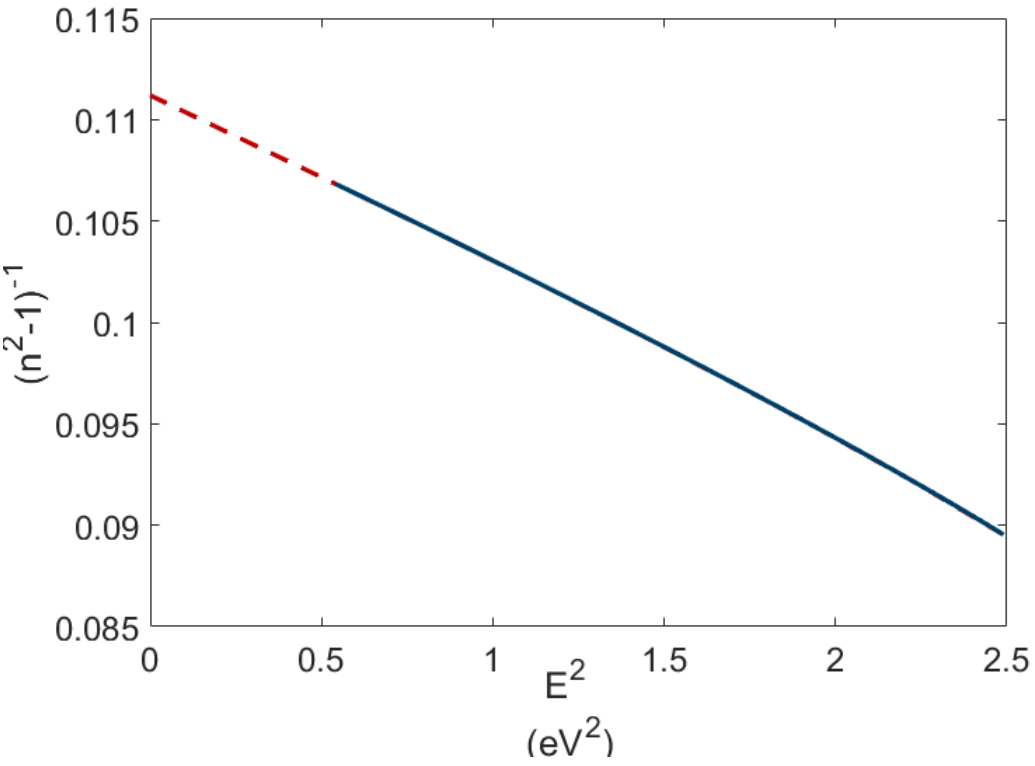

Figure 4.2: Extrapolation of refractive index in the IR region when the photon energy, E^2=0.

The refractive index used for calculating porosity is derived by the Equation 4.1 used by Wemple [67]. The rearrangement of this equation is used to compute refractive index. Equation 4.1 is the rearrangement of Equation 4.1. By plotting the data of refractive index obtained from SE according to the above relationship, it is seen that these data follow a linear relationship. From this linear relationship the refractive index at E^2=0 is obtained by extrapolation. This is seen in Fig 4.2.

$$n^2 - 1 = \frac{E_d E_0}{E_0^2 - E^2} \tag{4.1}$$

where,
E_d=dispersion energy
E_0=energy of the effective dispersion oscillator

$$\frac{1}{n^2 - 1} = a - bE^2 \tag{4.2}$$

4.2.2 Effective Medium Approximation models

As mentioned in Sub-section 4.2.1, porous silicon is considered as an effective medium. The various EMA models used to determine the effective refractive index of porous silicon are Bruggeman EMA, Maxwell-Garnett EMA and Looyenga EMA.

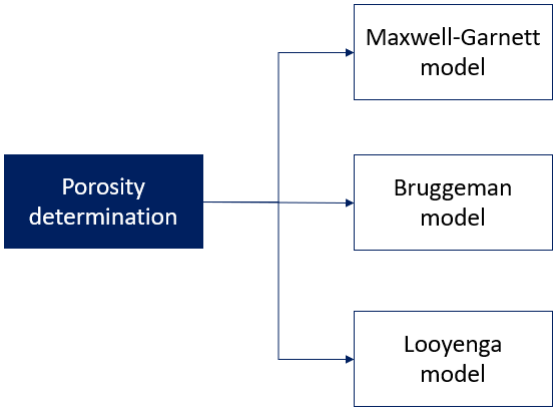

Figure 4.3: EMA models used to determine porosity.

According to Bergman's theory, porous silicon has a pore wall network, which is defined by percolation strength, g_0 [6][34]. This pore wall network is present even for large values of porosities making the percolation strength an important factor in selecting the appropriate EMA model [42]. If g_0 is zero then there is no percolation included in EMA models [42]. Bergman theory is valid for all EMA models.

- **Maxwell-Garnett model**
  Maxwell-Garnett model represents isolated silicon particles embedded in a vacuum matrix [69]. In such cases, the pore wall does not exist which means that the percolation strength is zero (g_0=0) [42]. Since porous silicon is a percolated system, Maxwell-Garnett method cannot be used. The Maxwell-Garnett formula is given by [44],

$$\frac{1-n_{\text{eff}}^2}{2+n_{\text{eff}}^2}+(1-P)\frac{\mathrm{n}_{\text{Si}}^2-1}{\mathrm{n}_{\text{Si}}^2+2}=0 \tag{4.3}$$

  where,
  n_{Si} represents the refractive index of bulk silicon.
  n_{eff} represents the effective refractive index of bulk silicon and voids.
  P represents the porosity of the material.

- **Looyenga model**
  As percolation strength exists for every value of porosity, the Looyenga model is applicable for high porosity values. The Looyenga formula to determine porosity is given by [43],

$$n_{\text{eff}}^{2/3}=(1-P)n_{\text{eff}}^{2/3}+P \tag{4.4}$$

- **Bruggeman model**
  This model is suitable for irregularly shaped particles [69] and is applicable for low porosities as the percolation strength becomes zero (g_0=0) for porosity values beyond 66.66% [42]. The Bruggeman formula used to calculate the porosity is given by [39],

$$P\frac{1-n_{\text{eff}}^2}{1-2n_{\text{eff}}^2}+(1-P)\frac{\mathrm{n}_{\text{Si}}^2-n_{\text{eff}}^2}{\mathrm{n}_{\text{Si}}^2+2n_{\text{eff}}^2}=0 \tag{4.5}$$

In this research, the model employed to calculate porosity is the Bruggeman EMA model. As discussed above, Bruggeman model is suitable for low porosities whereas the Looyenga model is suitable for high porosities. The Maxwell-Garnett model is not considered because of the the absence of percolated network. This selection of EMA model is further supported by Khardani [39] by comparing the porosity obtained by Bruggeman's approach with an independent measurement of porosity. The experimental and theoretical values of the refractive index as a function of porosity obtained by Khardani are shown in Fig 4.4. It can be seen that the theoretical and experimental values overlap in the low porosity region thus proving the use of Bruggeman EMA as the right choice.

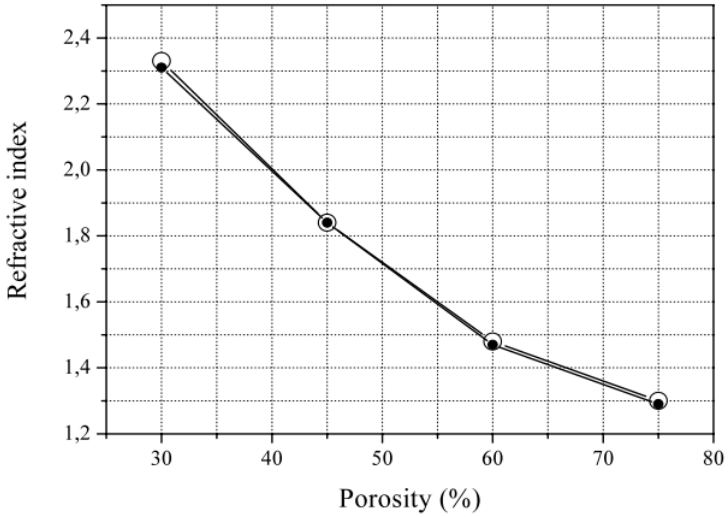

Figure 4.4: The experimental and theoretical values of the refractive index as a function of porosity as published by Khardani [39].

4.3 CONDUCTIVITY

The conductivity measured in section 3.3.2 is the conductivity of the bulk silicon. To calculate the effective conductivity where the voids and bulk material are considered a percolation model is adapted. As mentioned in Sub-section 4.2.2, porous silicon consists of a percolated network [42].

4.3.1 Percolation model

The percolation model considers the interconnection of the silicon network which contributes to the conductivity [26]. In this research, the percolation model considered for finding the effective electrical conductivity is based on the percolation model for determining effective thermal conductivity. This model applies to pores of different shapes (slip, spherical and cylindrical pores) [63]. The relationship between the porosity, percolation strength, conductivity of silicon and effective conductivity is described by [62],

$$\sigma_{eff} = \sigma_{\mathrm{Si}} f g_0 \tag{4.6}$$

where,
f =(1-P) denotes the volume fraction of the silicon with a porosity P
g_0 = volume fraction of silicon that is interconnected.

The interrelation between the g_0 and the volume fraction of the silicon (f) is given by,

$$g_0 = f^2 \tag{4.7}$$

Therefore, the final equation for calculating the effective electrical conductivity becomes,

$$\sigma_{eff} = \sigma_{\mathrm{Si}}(1-P)^3 \tag{4.8}$$

4.4 CONCLUSION FOR MODELS FOR POROUS A-SI:H

The refractive index of porous a-Si:H is measured in IR region as porous silicon is considered as an effective medium. Various EMA models like Bruggeman EMA, Maxwell-Garnett EMA, and Looyenga EMA models are available to determine the porosity of a-Si:H. In general, Bergman theory is valid for all EMA models. The Bergman theory includes the pore wall network with a percolation strength (g_0). Based on the percolation strength, the appropriate EMA model is selected. For this thesis, the selected EMA model is Bruggeman's model. The percolation strength is also considered for calculating the effective conductivity of a-Si:H.

5 MATERIAL CHARACTERIZATION

5.1 INTRODUCTION

The material properties of a-Si:H layer deposited by varying deposition power and deposition pressure is discusses in this chapter. From previous studies, the deposition rate is known to increase at high deposition power and decrease at high deposition pressure conditions [46]. Deposition at a low deposition rate produces dense structures, resulting in a high refractive index [7]. According to Gesele [26], conductivity decreases dramatically as porosity increases. The mentioned relationship between deposition conditions and material properties is mostly determined by altering deposition pressure or deposition power. Based on these results, the effect of varying both deposition power and deposition pressure is derived.

The first half of the chapter describes the the influence of PECVD deposition conditions on material properties. The latter half of the chapter focuses on understanding the relationship between PECVD deposition conditions and porosity, and the influence of dopant flow rate on porosity. As mentioned in Chapter 4, the porosity and effective conductivity are determined by using Bruggeman's Effective Medium Approach and percolation model, respectively. The sub-research questions are addressed in this chapter.

5.2 RESULTS

This section presents the variation in material properties as a function of deposition power and deposition pressure. It also includes the results of refractive index and conductivity as a function of dopant flow rate. The information obtained in this section is utilized to examine porosity as a function of deposition conditions and dopant flow rate.

5.2.1 Deposition rate as a function of deposition power and deposition pressure

As mentioned in Section 3.3.1, the thickness of the deposited layer is obtained from spectroscopic ellipsometry. The thickness and deposition time are used to compute the deposition rate (nm/min). This value is required to keep the thickness of the deposited anode under control. In addition, the flux of reactive species to the substrate during deposition is also reflected in the deposition rate and the flux of reactive species to a large extent determines the properties of the material [37][38].

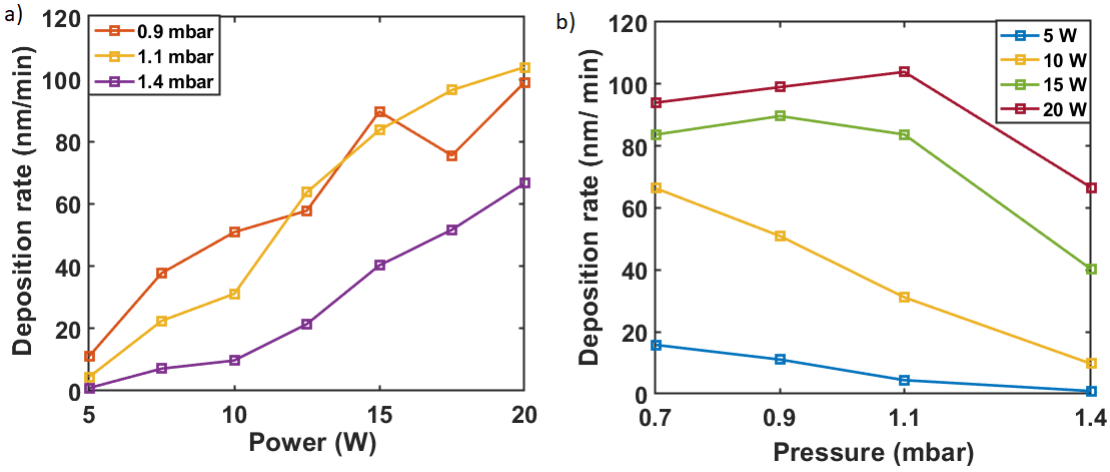

Figure 5.1: Deposition rate as a function of (a) deposition power and (b) deposition pressure.

The deposition rate as a function of deposition power at different values of pressure is displayed in Fig 5.1. It can be seen that the deposition rate increases as the power increases. The deposition rate significantly increases with power at low pressures (<1.1 mbar) when compared to high pressures (> 1.1 mbar). This is due of the effect of pressure, which is discussed in the next paragraph. The increase in deposition rate with deposition power is because of the availability of a large number of precursors [55], which results in increased gas dissociation, implying a higher flux of reactive species,leading to an increase of the deposition rate [37].

For low deposition pressure and high deposition power the deposition rate increases and after reaching an optimal value of pressure the deposition rate drops down. This is seen in Fig 5.1 b). As the pressure increases, the reactive species are packed more closely together thus shortening the distance between them [46] [38] [40]. This results in increased collision between reactive species that leads to both association and dissociation. Therefore, the deposition rate initially increases as pressure increases, and the ion bombardment with the substrate decreases due to high collisions at high pressures, resulting in a decrease in deposition rate.

5.2.2 Refractive index as a function of deposition power and deposition pressure

The refractive index of a material is high when it has a dense structure and low when it has voids [7]. Refractive index as a function of deposition power and deposition pressure is shown in Fig 5.2. This figure shows that the refractive index decreases with deposition power. It can be observed that refractive index is mainly dependent on deposition power as the refractive index remains almost the same for deposition pressure settings.

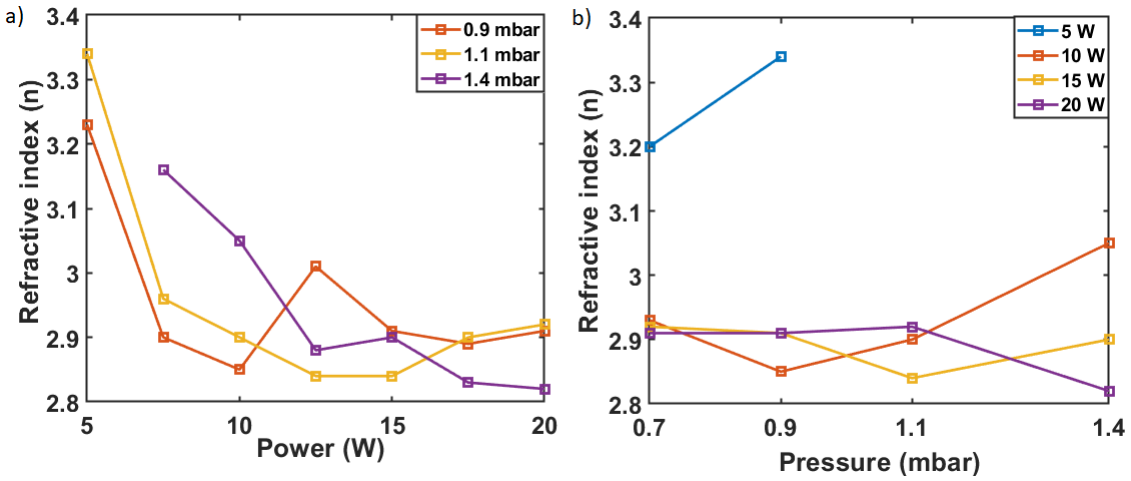

Figure 5.2: Refractive Index as a function of (a) deposition power and (b) deposition pressure.

5.2.3 Conductivity as a function of deposition power and deposition pressure

The conductivity of a-Si:H as a function of deposition power and deposition pressure is shown in Fig 5.3. The conductivity tends to decrease at high values of deposition power. It is obvious because the void formation is high at high deposition power. Conductivity as a function of deposition pressure shows that there is a slight increase with pressure. This is especially true at low deposition power values. Hence, the conductivity increases for deposition conditions such as low deposition power and high deposition pressure.

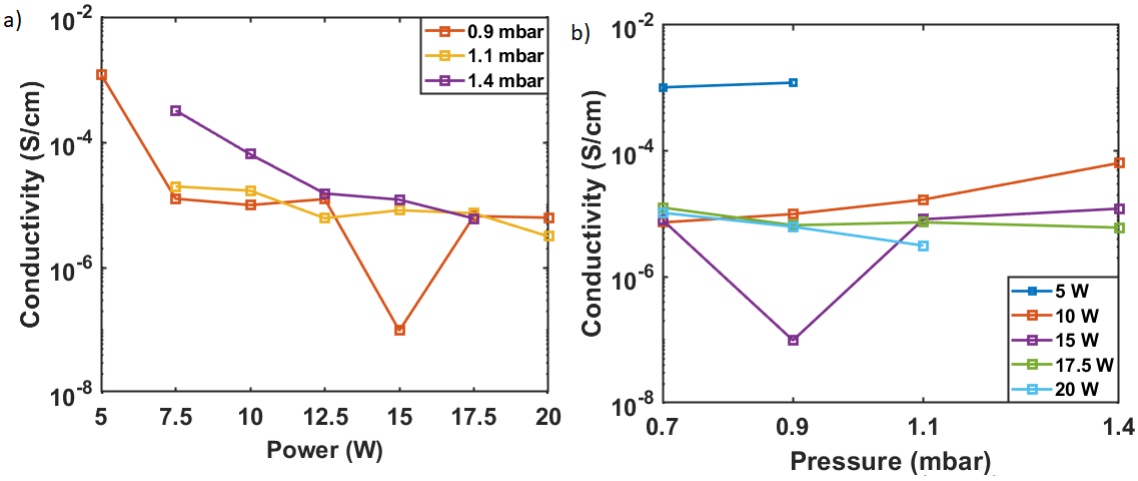

Figure 5.3: Conductivity as a function of (a) deposition power and (b) deposition pressure.

5.2.4 Refractive index as a function of dopant flow rate

The refractive index as a function of dopant flow rate (PH_3) is shown in Fig 5.4. The refractive index is seen to decrease somewhat as the dopant flow rate increases. This indicates that the voids in the deposited film increases as the concentration of PH_3 increases.

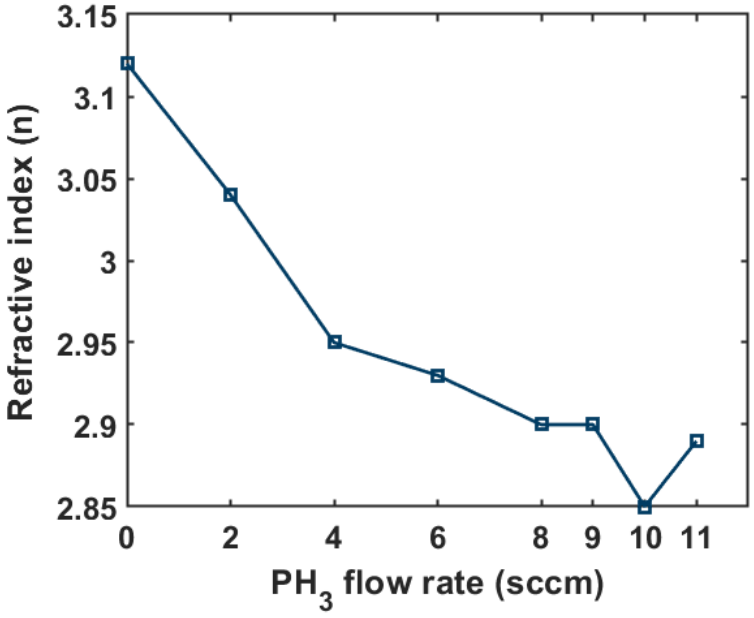

Figure 5.4: Refractive index as a function of dopant flow rate.

5.2.5 Conductivity as a function of dopant flow rate

According to Carlson, adding dopant enhances conductivity by ten orders of magnitude, and the deposition of dopant is faster than the deposition of silicon, thus even a little increase in dopant flow rate can boost conductivity [9]. It can be seen from Fig 5.5 that the conductivity increases with the increase in dopant flow rate.

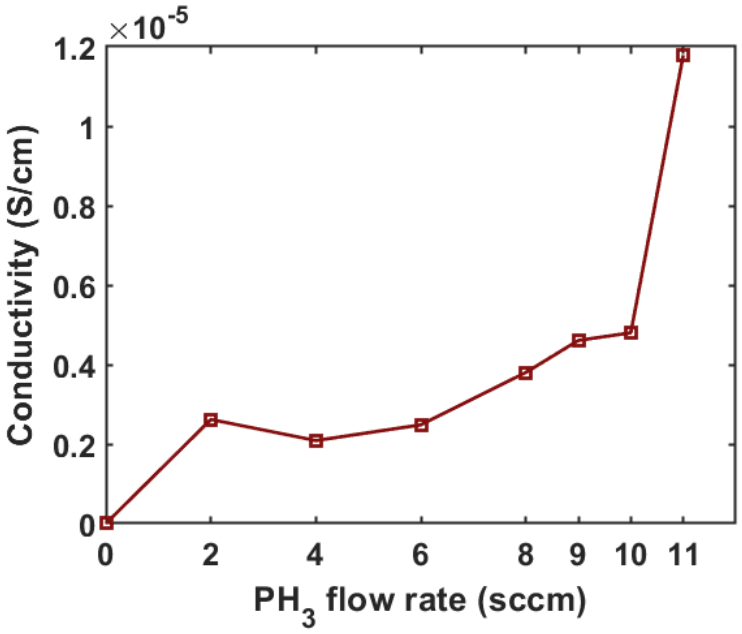

Figure 5.5: The conductivity as a function of the PH_3 flow.

5.3 DISCUSSION

The results reported in Section 5.2 are discussed in this section. This section answers the sub-research questions mentioned in Section 1.3.2.

5.3.1 Influence of PECVD deposition conditions on porosity

Porosity is the ratio of empty pore volume to the total volume [42]. The porosity of each sample was calculated using Bruggeman's Effective Medium approach as mentioned in Sub-section 4.2.1. Porosity as a function of deposition power and deposition pressure is visible in Fig 5.6 and its contour is represented in Fig 5.7.

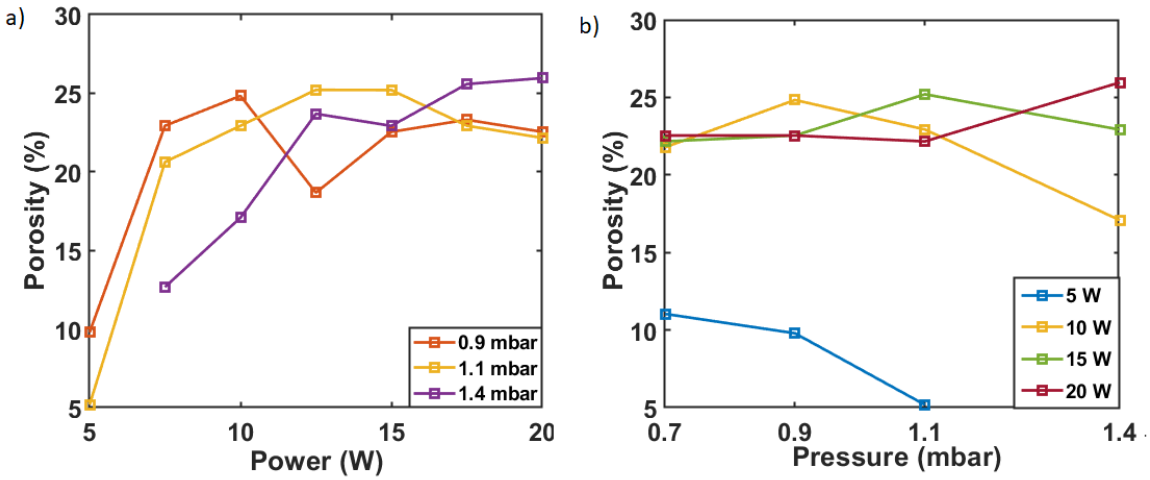

Figure 5.6: Porosity as a function of (a) deposition power and (b) deposition pressure.

It is seen that the porosity is at its highest at high deposition power and high deposition pressure, and low at low deposition power and high deposition pressure. In general, the porosity is high at high deposition power.

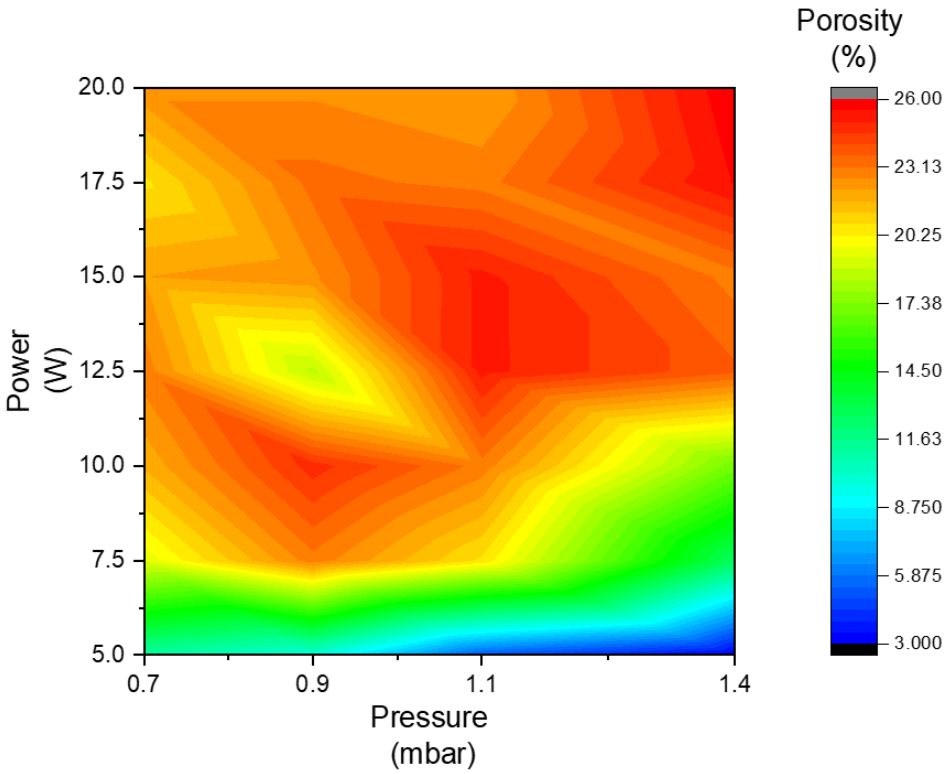

Figure 5.7: Porosity as a function of power and pressure.

5.3.2 Porosity as a function of refractive index

The refractive index is computed to calculate the porosity using Bruggeman's Effective Medium approach. The porosity of a-Si:H decreases as the refractive index increases. The fluctuation in porosity caused by a minor change in refractive index is depicted in Fig 5.8.

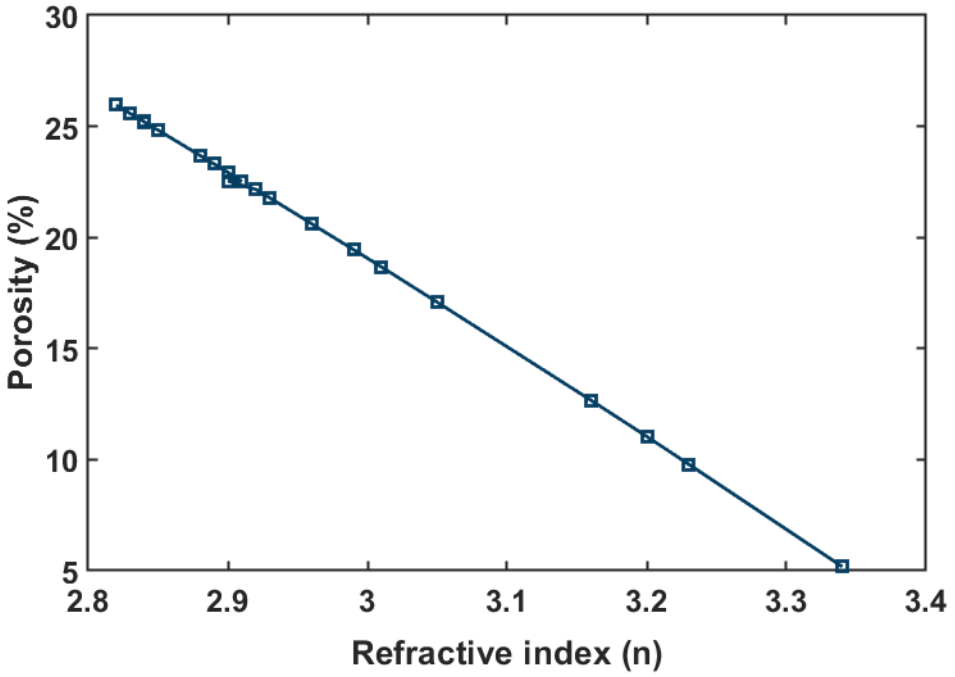

Figure 5.8: Porosity as a function of refractive index.

5.3.3 Influence of dopant flow rate on porosity

Doping increases the defect density by forming vacancies, voids or dangling bonds and the incorporation of hydrogen reduces the defect density [9][59]. It is seen in Fig 5.9 that as the concentration of PH_3 (dopant) increases, the porosity increases.

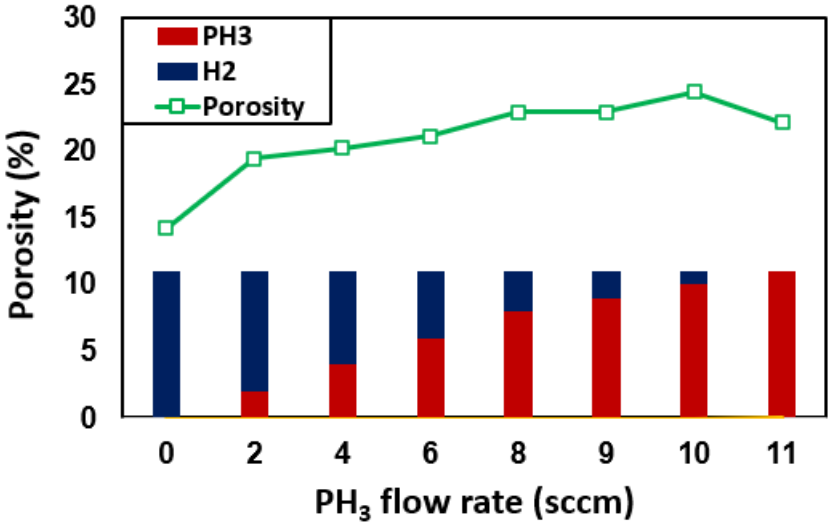

Figure 5.9: Porosity as a function of PH_3 concentration. The blue bar represents the H_2 concentration and the red bar represents the PH_3 concentration. The flow rate of both the gases (PH_3+H_2) sums up to 11 sccm.

5.3.4 Porosity as a function of deposition rate

According to Section 5.2.1, the deposition rate contributes to the density of the film. Fig 5.10 shows the porosity as a function of deposition rate when both power (left) and pressure (right) are varied.

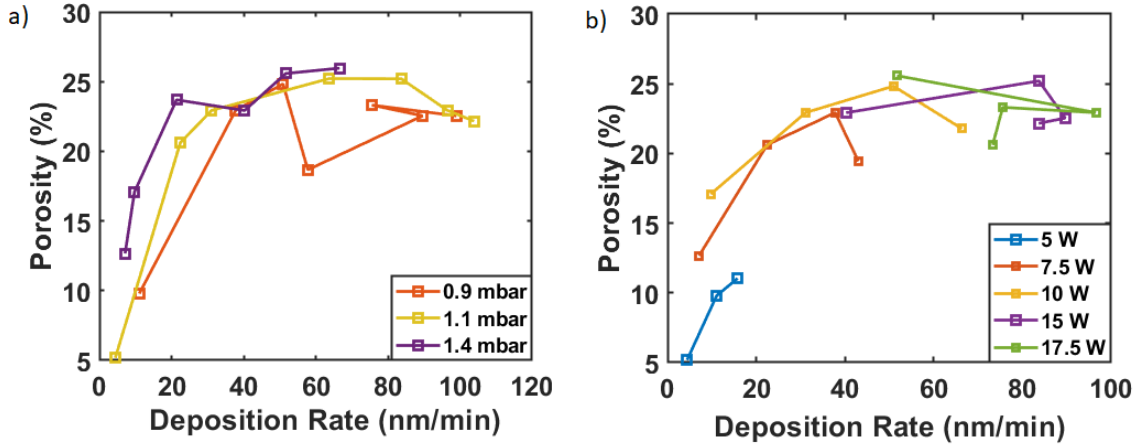

Figure 5.10: Porosity as a function of deposition rate when (a) deposition power and (b) deposition pressure is varied.

As observed in the Fig 5.10 (a), the porosity increases as the deposition rate increases. This is because the deposition rate increases as power increases. Since the deposition rate decreases after an optimum value of pressure, the increase in deposition rate beyond this optimum pressure does not cause a significant increase in porosity. The porosity is also seen to decrease as the deposition pressure further increases. Thus, the porosity is seen to decrease as deposition rate increases. This is seen in Fig 5.10 (b).

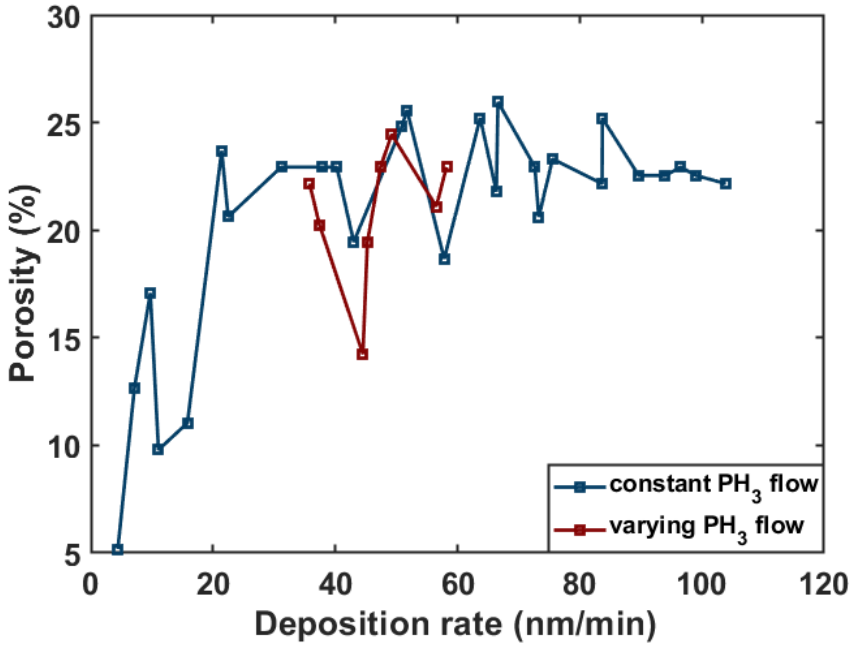

Figure 5.11: Porosity as a function of deposition rate for all deposition conditions.

It can be seen in Fig 5.11 that the porosity increases with an increase in the deposition rate when the dopant flow rate is kept constant. This is because the radicals of the precursor SiH_4 contributing to the film growth at low deposition rates form high quality films and at high deposition rates, the radicals form voids in the film [61][24][3]. However, the porosity is not dependent on the deposition rate when dopant gas flow rate is varied. This could be because of the addition of hydrogen gas as mentioned in Sub-section 3.2.1. As a result, the porosity of varying dopant flow rate is dependent on the dopant flow rate and not on the depositon rate.

5.3.5 Conductivity as a function of porosity

As seen in Fig 5.12, the conductivity decreases with the increase in porosity. This is because the voids inside the material do not absorb electrons [20]. Hence, as the number of voids i.e. porosity increases the conductivity decreases. This stands true only when the PH_3 flow rate is constant. From Sub-section 5.2.5 it is clear that the conductivity increases with PH_3 flow rate. Fig 5.12 also includes the conductivity as a function of porosity when PH_3 flow rate is varied. It can be seen that both conductivity and porosity increase with an increase in PH_3 flow rate.

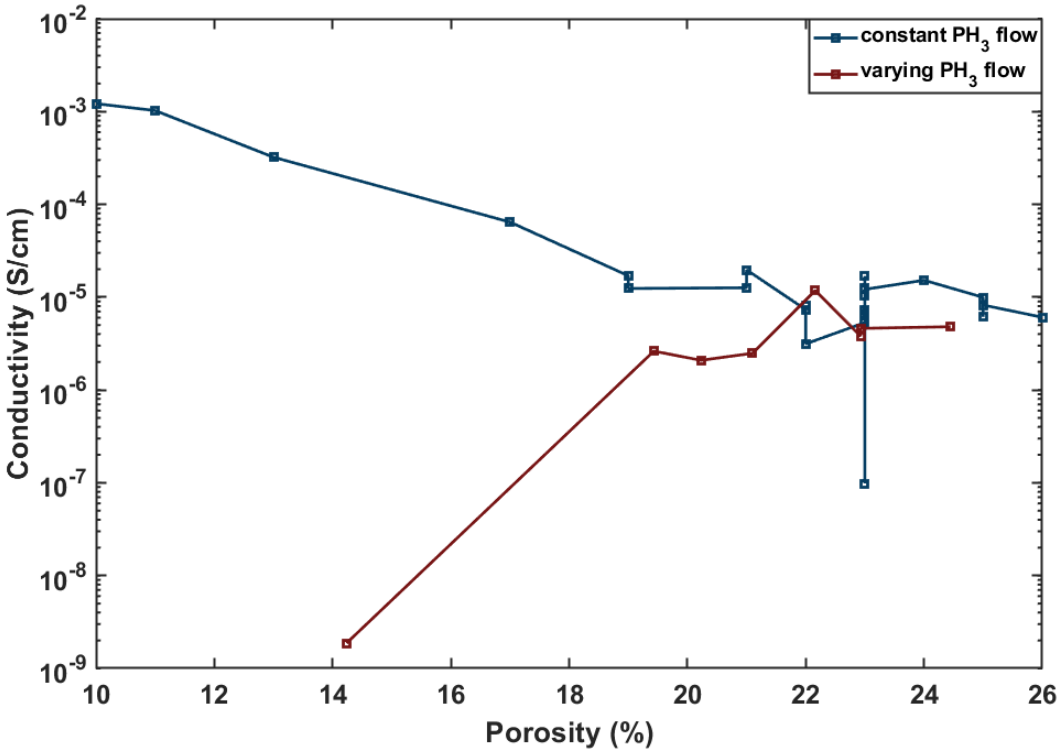

Figure 5.12: Conductivity as a function of porosity.

5.4 CONCLUSION FOR MATERIAL CHARACTERIZATION

The deposition rate increases for deposition conditions such as high power and low pressure. High deposition rate results in the formation of voids and low deposition rate results in a much dense film i.e. less number of voids [61][24][3]. Hence, the refractive index of the deposited film decreases at high deposition power and low deposition pressure. To increase the conductivity of the deposited film the deposition settings used must be low deposition power and high deposition pressure.

The porosity of the film was determined by using the Bruggeman Effective Medium Approach. This results in an increase in porosity for the same deposition settings that decrease the refractive index. If the porosity of the film is high then the conductivity of the film is low. Same value of porosity can be obtained by varying the deposition conditions. Even though the the porosity is same, the conductivity varies. According to Saha et al., this could be because the reaction of dopant with the substrate depends on the deposition conditions [55].

When the dopant flow rate is varied by keeping the deposition power and deposition pressure constant, the refractive index of the deposited film decreases as the dopant flow rate increases. The refractive index is low at high dopant flow rate because the defect density increases with doping whereas, the refractive index is high at low dopant flow rate because of the the presence of H_2 gas. However, the conductivity of the deposited film is low at low dopant flow rate and the conductivity increases with an increase in dopant flow rate.

The increase in dopant flow rate causes an increases in the porosity of the deposited film as doping increases both conductivity and defect density.

6 BATTERY DISCHARGE RESULTS

6.1 INTRODUCTION

The a-Si:H anode prepared in Sub-section 3.2 are utilized in comparing the discharge performance of silicon-air battery with c-Si as anode. First, the discharge experiments of silicon-air battery were conducted by using p-type c-Si wafer as anode, KOH as electrolyte and porous carbon electrode as cathode. The surface area of the electrodes was 1 cm2. The electrochemical galvanostatic discharge experiments were carried out using a galvanostat, Autolab. Finally, the a-Si:H anode was used for discharging the battery. The use of a-Si:H is expected to increase the specific discharge capacity of the battery. During the discharge of silicon-air battery, there were some experimental problems faced. This chapter presents an overview of the experiments and the attempts to solve the problem.

6.2 BATTERY DISCHARGE USING C-SI AS ANODE

The silicon-air cell was setup as mentioned in Section 3.4. The discharge experiments using c-Si as anode were carried out to reproduce the results of Prins [51]. Firstly, the type of anode, electrolyte concentration, and pre-wetting time of cathode were replicated as Prins's [51] experiments to obtain similar discharge curves. The discharge current density applied was 150 $\mu A/cm^2$ However, it was difficult to reproduce similar discharge curves. To overcome this problem, several alterations were made to the battery. One of the solutions considered was to vary the concentration of KOH from 0% to 60% to examine whether the battery showed any discharge. Unfortunately, the battery did not show any discharge. Therefore, 30% KOH solution as was used by Prins was considered.

Next, the discharge current density was varied to examine the discharge curve. Since previous literature reports low discharge current density between 7.9 $\mu A/cm^2$ and 50 $\mu A/cm^2$, a low discharge current density was used. Thus, a discharge current density of 7.9 $\mu A/cm^2$ and 50 $\mu A/cm^2$ was applied. The battery was kept in open-circuit condition for 300 seconds. It confirmed the discharge of the battery. However, the discharge curves were not the same as the discharge curves of Prins [51]. These discharge curves are shown in Fig 6.1. It can be seen that the the discharge curve for 7.9 $\mu A/cm^2$ continues over 24 hours, whereas the discharge curve for 50 $\mu A/cm^2$ is seen to decline faster. For this reason, a discharge current density of 7.9 $\mu A/cm^2$ was used to discharge all the further experiments.

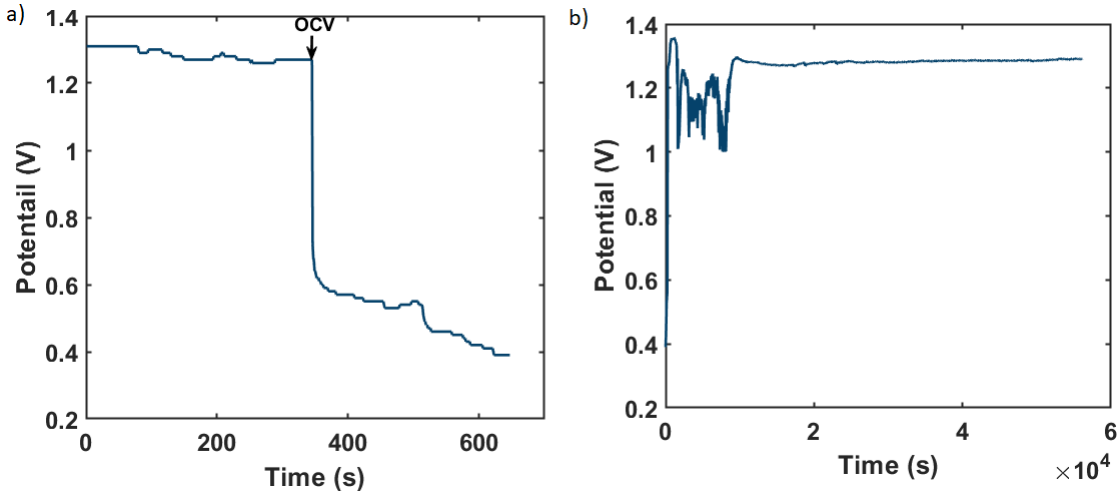

Figure 6.1: Discharge curve of a silicon-air battery with a discharge current density of 50 $\mu A/cm^2$. The OCV time was 300 seconds.

During the middle of this research, the equipment used for discharging the battery was moved from MEMS lab to Cleanroom 10000 at EKL. This caused a problem with the circuit connection and all the discharge experiments carried out were not successful. The OCV was seen to increase beyond the expected potential which is 1-1.4 V and reached a value of 10 V. This increase in OCV is seen in Fig 6.2. After contacting the process owner, this problem was assumed to be solved as the discharge of a 9 V battery was successful and exhibited a voltage of 9 V when the current was applied. Therefore, the discharge experiments of silicon-air battery were continued. However, the discharge of silicon-air battery was not accomplished. The next step considered was to use a-Si:H as anode.

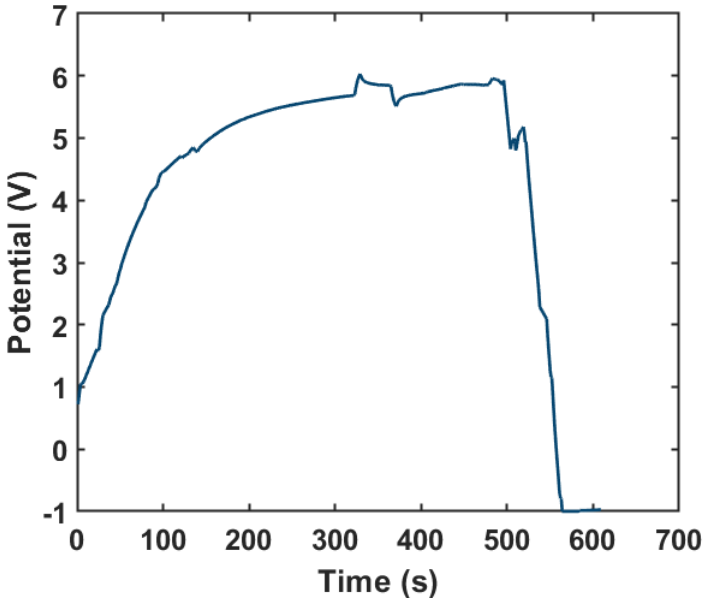

Figure 6.2: Discharge curve of a silicon-air battery with a discharge current density of 7.9 $\mu A/cm^2$. The OCV time was 600 seconds.

6.3 BATTERY DISCHARGE USING A-SI:H AS ANODE

The silicon-air battery was discharged using intrinsic a-Si:H as anode. Because of the internal resistance the discharge potential was low. This internal resistance can be reduced by doping and, hence, n-type a-Si:H was used as anode. First, the n-type a-Si:H on Asahi with Al back contact was used as anode. The discharge of such a battery was not achieved. Since Garamoun et al. used Al contact at the front and back side of the anode, similar type of anode was adapted.

It was noticed that the a-Si:H was quickly dissolved in KOH solution. The complete consumption of a-Si:H anode is displayed in Fig 6.3. Therefore, the OCV time of the battery was reduced to 300 seconds.

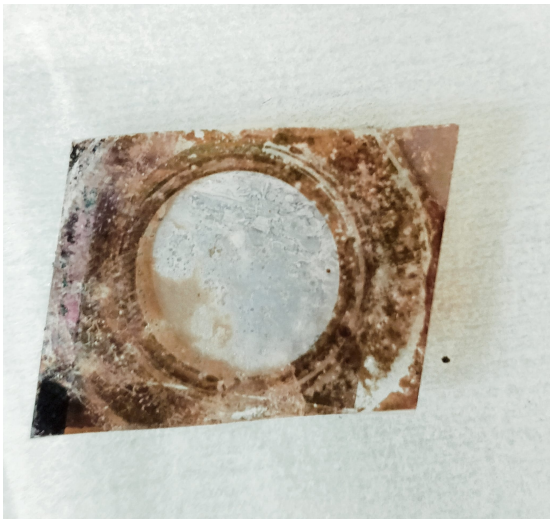

Figure 6.3: The dissolution of a-Si:H in KOH solution.

The battery was discharged at a discharge current density of 7.9 $\mu A/cm^2$ for KOH concentration of 6 M and 0.01 M. The battery showed a discharge at 0.01 M and at 6 M the cell potential dropped to zero. Hence, the KOH concentration used was 0.01 M, which is similar to what Garamoun et al. used. The discharge curves for silicon-air battery using KOH concentrations of 6 M and 0.01 M is shown in Fig 6.4.

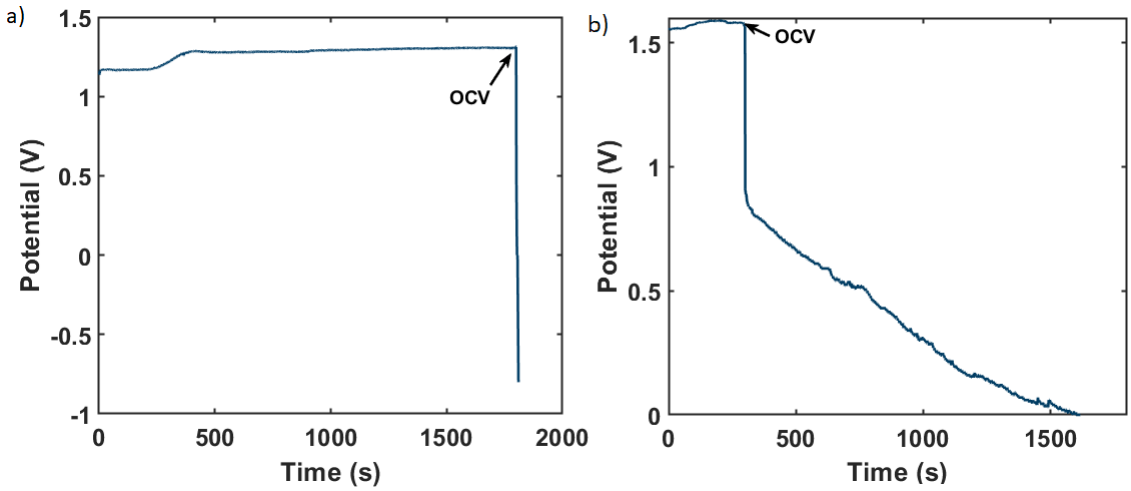

Figure 6.4: Discharge curve of a silicon-air battery with a discharge current density of 7.9 $\mu A/cm^2$ and KOH concentration of 6 M. The OCV time was 1800 seconds.

After obtaining a discharge curve for n-type a-Si:H anode, the discharge experiments were conducted for n-type a-Si:H anode of different porosities. Unfortunately, the battery did not display a discharge curve. The potential of the silicon-air battery immediately dropped to zero. To confirm the discharge of the silicon-air battery, the concentration of KOH was varied at 0.01 M, 0.05 M and 0.1 M. Even at different concentrations of KOH the battery did not discharge.

According to Guo [32], the addition of additives in electrolyte delays the passivation reaction, which contributes to the discharge of the battery. Hence, ethanol was used as an additive in KOH solution. The battery discharge experiments carried out using an additive showed a delay of few seconds (3-5 seconds) before the potential reached zero.

Since the use of additives helps with the performance of the battery, the electrolyte used by Prins was investigated to verify the contents of the pre-mixed KOH solution. The datasheet of pre-mixed KOH solution used by Prins contains other elements along with KOH and water. This data sheet is presented in Fig 6.5. The prominent element was 1% carbonate. According to Renuka [54], the presence of carbonate plays an important role in delaying the passivation. Therefore, it is recommended to carry out further discharge experiments using carbonate in KOH solution to investigate the performance of silicon-air battery.

Specifications

Carbonate	1% max.
Chloride	0.01% max.
Chlorate	0.01% max.
Density	1.510g/cm³
Identification	Pass Test
Heavy Metals (as Pb)	0.002% max.
Iron (Fe)	5ppm max.
Physical Form	Liquid
Percent Purity	29.5 to 30.5%
Mercury (Hg)	1ppm max.

Figure 6.5: The data sheet of pre-mixed KOH solution by Fischer Chemical.

6.4 CONCLUSION FOR BATTERY DISCHARGE RESULTS

The silicon-air battery using c-Si and a-Si:H as anode was discharged. The discharge curve for c-Si anode was achieved for a discharge current density of 7.9 $\mu A/cm^2$ and KOH concentration of 30% in water instead of a discharge current density of 150 $\mu A/cm^2$ that Prins used [51]. This was followed by using a-Si:H anode for the discharge of silicon-air battery. The intrinsic a-Si:H anode has high internal resistance hence, the doped n-type a-Si:H anode is used. However, the n-type a-Si:H did not discharge using 30% KOH. Therefore, the KOH concentration employed to discharge the silicon-air battery was 0.01 M. The discharge time for such a battery was 1600 seconds. However, the discharge experiments of silicon-air battery using a-Si:H as anode were not successful. The reasons for this could be that the silicon in a-Si:H anode dissolves quickly in KOH solution, the transfer of the equipment, and the presence of carbonate or additional elements in the pre-mixed KOH solution that were absent in the manually prepared KOH solution using pellets.

7 CONCLUSION

The focus of this research is to reduce the effect of passivation during discharge of silicon-air battery. According to the research by Zhong et al., Park et al., and Garamoun et al. [74][48][25], increasing the anode's surface area is a preferred method for delaying the passivation reaction and increasing the specific discharge capacity. As a result, the surface area of the silicon anode is altered in this study by altering its porosity using the PECVD process.

To create silicon anodes with variable porosities, the deposition conditions are adjusted. For this reason it is important to investigate and understand the relationship between these deposition settings on porosity. Firstly, the deposition conditions such as deposition power and deposition pressure are varied and the remaining conditions are kept constant. It was observed that when the deposition power increases, so does the deposition rate. This deposition rate is critical in determining the properties of the deposited material as deposition rate determines the density of the deposited layer. A high deposition rate leads to formation of voids in the material. Thus, at high deposition power, the deposition rate increases and refractive index decreases. The conductivity of the deposited layer decreases at high deposition power and low deposition pressure. Although both deposition power and deposition pressure can be changed, deposition power has the greatest impact on the qualities of the deposited material.

The porosity of the film was determined by using the Bruggeman Effective Medium Approach. The refractive index was derived as a means to find porosity. Porosity is increased by using deposition conditions that lower the refractive index. When the porosity of the film is high, the conductivity of the film is poor.

Finally, the dopant flow rate is changed while other deposition conditions remain the same. This results in the decrease of refractive index as the dopant flow rate increases. Doping is known to improve conductivity, therefore as the concentration of dopant increases, so does the conductivity. Additionally, an increase in dopant flow rate induces an increase in the porosity of the deposited film.

After the depositions of silicon anode of various porosities, the silicon-air battery was discharged by using c-Si and a-Si:H as anode. The discharge of the battery was possible for low discharge current densities rather than a high discharge current density used by Prins. The concentration of KOH used to discharge a silicon-air battery utilizing c-Si was 6.91 M, but it was 0.01 M for a-Si:H. Unfortunately, the discharge experiments with a-Si:H as anode in

a silicon-air battery were unsuccessful. It seems that the problem lies within the electrolyte as KOH pellets were used instead of pre-mixed KOH solution that contained carbonate and other elements. Other factors could include the equipment transfer, which could have caused some circuit damage, and the rapid dissolving of a-Si:H in KOH solution. As a result, no definitive conclusion about the effect of porosity on the discharge of a silicon-air battery can be drawn.

7.1 RECOMMENDATIONS

Based on the process, the results and the analysis of the research, a set of recommendations are listed.

1. Since porosity varies by varying deposition power and deposition pressure, other deposition parameters such as temperature or SiH_4 flow rate can also be varied to understand the influence of PECVD deposition parameters on porosity and properties of the material.

2. According to Garamoun et al. [25], the specific discharge capacity is highest for a-SiC anode than a-Si:H because the silicon consumed for the discharge is 7% for a-SiC and 5% for a-Si:H. Hence, the anode must be alloyed with carbon and the discharge of silicon-air battery should be investigated using a-SiC as anode.

3. The pre-mixed KOH solution could discharge the silicon-air battery which suggests that the presence of other elements play a role. In order to reduce passivation, electrolyte additives such as ethanol, carbonate and acetate should be investigated.

BIBLIOGRAPHY

1. Agreement, P. (2015). Paris agreement. In *Report of the Conference of the Parties to the United Nations Framework Convention on Climate Change (21st Session, 2015: Paris). Retrived December*, volume 4, page 2017. HeinOnline.

2. Aneke, M. and Wang, M. (2016). Energy storage technologies and real life applications–a state of the art review. *Applied Energy*, 179:350–377.

3. Ballutaud, J. (2004). Study of radio-frequency plasma deposition of amorphous silicon for the improvement of solar cell production. Technical report, EPFL.

4. Bansal, R., Menon, P., and Sharma, R. (2020). Silicon–air batteries: progress, applications and challenges. *SN Applied Sciences*, 2:1–17.

5. Bard, A. J., Faulkner, L. R., et al. (2001). Fundamentals and applications. *Electrochemical methods*, 2(482):580–632.

6. Bergman, D. J. (1978). The dielectric constant of a composite material—a problem in classical physics. *Physics Reports*, 43(9):377–407.

7. Cabarrocas, P. R. i. (1994). Deposition of intrinsic, phosphorus-doped, and boron-doped hydrogenated amorphous silicon films at 50° c. *Applied physics letters*, 65(13):1674–1676.

8. Canham, L. (2014). *Handbook of porous silicon*. Springer.

9. Carlson, D., Smith, R., Magee, C., and Zanzucchi, P. (1982). The role of hydrogen in heavily doped amorphous silicon. *Philosophical Magazine B*, 45(1):51–68.

10. Cattarin, S. and Musiani, M. M. (1999). Electrodissolution and passivation of silicon in aqueous alkaline media: A voltammetric and impedance investigation. *The Journal of Physical Chemistry B*, 103(16):3162–3169.

11. Cheng, F. and Chen, J. (2012). Metal–air batteries: from oxygen reduction electrochemistry to cathode catalysts. *Chemical Society Reviews*, 41(6):2172–2192.

12. Coffinier, Y., Piret, G., Das, M. R., and Boukherroub, R. (2013). Effect of surface roughness and chemical composition on the wetting properties of silicon-based substrates. *Comptes Rendus Chimie*, 16(1):65–72.

13. Cohn, G., Altberg, A., Macdonald, D. D., and Ein-Eli, Y. (2011a). A silicon–air battery utilizing a composite polymer electrolyte. *Electrochimica acta*, 58:161–164.

14. Cohn, G., Eichel, R. A., and Ein-Eli, Y. (2013). New insight into the discharge mechanism of silicon–air batteries using electrochemical impedance spectroscopy. *Physical chemistry chemical physics*, 15(9):3256–3263.

15. Cohn, G. and Ein-Eli, Y. (2010). Study and development of non-aqueous silicon-air battery. *Journal of Power Sources*, 195(15):4963–4970.

16. Cohn, G., Macdonald, D. D., and Ein-Eli, Y. (2011b). Remarkable impact of water on the discharge performance of a silicon–air battery. *ChemSusChem*, 4(8):1124–1129.

17. Cohn, G., Starosvetsky, D., Hagiwara, R., Macdonald, D. D., and Ein-Eli, Y. (2009). Silicon–air batteries. *Electrochemistry Communications*, 11(10):1916–1918.

18. Durmus, Y. E. (2013). *Modeling of silicon-air batteries*. PhD thesis, University of Ulm.

19. Durmus, Y. E., Aslanbas, Ö., Kayser, S., Tempel, H., Hausen, F., De Haart, L., Granwehr, J., Ein-Eli, Y., Eichel, R.-A., and Kungl, H. (2017). Long run discharge, performance and efficiency of primary silicon–air cells with alkaline electrolyte. *Electrochimica acta*, 225:215–224.

20. Fanni, L., Delaup, B., Niesen, B., Milstein, Y., Shachal, D., Morales-Masis, M., Nicolay, S., and Ballif, C. (2015). Tuning the porosity of zinc oxide electrodes: from dense to nanopillar films. *Materials Research Express*, 2(7):075006.

21. Ferlauto, A., Ferreira, G., Pearce, J. M., Wronski, C., Collins, R., Deng, X., and Ganguly, G. (2002). Analytical model for the optical functions of amorphous semiconductors from the near-infrared to ultraviolet: Applications in thin film photovoltaics. *Journal of Applied Physics*, 92(5):2424–2436.

22. Fujiwara, H. (2007). *Spectroscopic ellipsometry: principles and applications*. John Wiley & Sons.

23. Fujiwara, H. and Collins, R. W. (2018). *Spectroscopic ellipsometry for photovoltaics*, volume 1. Springer.

24. Gallagher, A. (1988). Neutral radical deposition from silane discharges. *Journal of applied physics*, 63(7):2406–2413.

25. Garamoun, A., Schubert, M. B., and Werner, J. H. (2014). Thin-film silicon for flexible metal–air batteries. *ChemSusChem*, 7(12):3272–3274.

26. Gesele, G., Linsmeier, J., Drach, V., Fricke, J., and Arens-Fischer, R. (1997). Temperature-dependent thermal conductivity of porous silicon. *Journal of Physics D: Applied Physics*, 30(21):2911.

27. Gilliam, R., Graydon, J., Kirk, D., and Thorpe, S. (2007). A review of specific conductivities of potassium hydroxide solutions for various concentrations and temperatures. *International Journal of Hydrogen Energy*, 32(3):359–364.

28. Glembocki, O. J., Palik, E. D., de Guel, G. R., and Kendall, D. L. (1991). 138(4):1055–1063.

29. Goodenough, J. B. and Kim, Y. (2010). Challenges for rechargeable li batteries. *Chemistry of materials*, 22(3):587–603.

30. Gope, J., Kumar, S., Parashar, A., Dixit, P., Rauthan, C., Panwar, O., Patel, D., and Agarwal, S. (2009). Amorphous and nanocrystalline silicon made by varying deposition pressure in pecvd process. *Journal of non-crystalline solids*, 355(45-47):2228–2232.

31. Grubb, M., Vrolijk, C., and Brack, D. (1999). The kyoto protocol: a guide and assessment.

32. Guo, S., Qin, L., Zhang, T., Zhou, M., Zhou, J., Fang, G., and Liang, S. (2020). Fundamentals and perspectives of electrolyte additives for aqueous zinc-ion batteries. *Energy Storage Materials*.

33. Hardwick, L. J. and De León, C. P. (2018). Rechargeable multi-valent metal-air batteries. *Johnson Matthey Technology Review*, 62(2):134–149.

34. Helbig, R. (1994). *Festkörperprobleme 34*, volume 34.

35. Hosseini, S., Han, S. J., Arponwichanop, A., Yonezawa, T., and Kheawhom, S. (2018). Ethanol as an electrolyte additive for alkaline zinc-air flow batteries. *Scientific reports*, 8(1):1–11.

36. Ibrahim, H., Ilinca, A., and Perron, J. (2008). Energy storage systems—characteristics and comparisons. *Renewable and sustainable energy reviews*, 12(5):1221–1250.

37. Iliescu, C., Avram, M., Chen, B., Popescu, A., Dumitrescu, V., Poenar, D., Sterian, A., Vrtacnik, D., Amon, S., and Sterian, P. (2011). Residual stress in thin films pecvd depositions. *Journal of Optoelectronics and Advanced Materials*, 13(4):387–394.

38. Iliescu, C. and Chen, B. (2007). Thick and low-stress pecvd amorphous silicon for mems applications. *Journal of Micromechanics and Microengineering*, 18(1):015024.

39. Khardani, M., Bouaïcha, M., and Bessaïs, B. (2007). Bruggeman effective medium approach for modelling optical properties of porous silicon: comparison with experiment. *physica status solidi c*, 4(6):1986–1990.

40. Kim, D. Y., Guijt, E., van Swaaij, R. A., and Zeman, M. (2015). Development of a-siox: H solar cells with very high voc$\times$ ff product. *Progress in Photovoltaics: research and applications*, 23(6):671–684.

41. Lavareda, G., Vygranenko, Y., Amaral, A., de Carvalho, C. N., Barradas, N., Alves, E., and Brogueira, P. (2021). Dependence of optical properties on composition of silicon carbonitride thin films deposited at low temperature by pecvd. *Journal of Non-Crystalline Solids*, 551:120434.

42. Lockwood, D. (1994). Optical properties of porous silicon. *Solid State Communications*, 92(1-2):101–112.

43. Looyenga, H. (1965). Dielectric constants of heterogeneous mixtures. *Physica*, 31(3):401–406.

44. MAXWELL-GARNETT, J. C. (1904). Colours in metal glasses and in metallic films. *Phil. Trans. R. Soc. Lond, A*, 203:385–420.

45. Niklasson, G. A., Granqvist, C., and Hunderi, O. (1981). Effective medium models for the optical properties of inhomogeneous materials. *Applied Optics*, 20(1):26–30.

46. Ong, Y. Y., Chen, B. T., Tay, F. E., and Iliescu, C. (2006). Process analysis and optimization on pecvd amorphous silicon on glass substrate. In *Journal of Physics: Conference Series*, volume 34, page 134. IOP Publishing.

47. Osseo-Asare, K., Wei, D., and Mishra, K. K. (1996). Dissolution windows for wet chemical processing of silicon and silicon dioxide: Potential-ph diagrams for the si-f-h 2 o system. *Journal of the Electrochemical Society*, 143(2):749.

48. Park, D.-W., Kim, S., Ocon, J. D., Abrenica, G. H. A., Lee, J. K., and Lee, J. (2015). Controlled electrochemical etching of nanoporous si anodes and its discharge behavior in alkaline si–air batteries. *ACS applied materials & interfaces*, 7(5):3126–3132.

49. Peters, J. F. and Weil, M. (2016). A critical assessment of the resource depletion potential of current and future lithium-ion batteries. *Resources*, 5(4):46.

50. Potyrailo, R. A. and Amis, E. J. (2003). Elements of high-throughput analysis in combinatorial materials science. In *High-Throughput Analysis*, pages 1–13. Springer.

51. Prins, J. (2020). Alkaline pre-treatment of the air electrode in a silicon-air battery.

52. Rahman, M. A., Wang, X., and Wen, C. (2013). High energy density metal-air batteries: a review. *Journal of the Electrochemical Society*, 160(10):A1759.

53. Ravindra, N. and Narayan, J. (1986). Optical properties of amorphous silicon and silicon dioxide. *Journal of applied physics*, 60(3):1139–1146.

54. Renuka, A., Veluchamy, A., and Venkatakrishnan, N. (1991). Effect of carbonate ions on the behaviour of zinc in 30% koh. *Journal of power sources*, 34(4):381–385.

55. Saha, S., Barua, A., and Ray, S. (1993). The role of hydrogen dilution and radio frequency power in the formation of microcrystallinity of n-type si: H thin film. *Journal of applied physics*, 74(9):5561–5568.

56. See, D. M. and White, R. E. (1997). Temperature and concentration dependence of the specific conductivity of concentrated solutions of potassium hydroxide. *Journal of Chemical & Engineering Data*, 42(6):1266–1268.

57. Seidel, H., Csepregi, L., Heuberger, A., and Baumgärtel, H. (1990). Anisotropic etching of crystalline silicon in alkaline solutions: I. orientation dependence and behavior of passivation layers. *Journal of the electrochemical society*, 137(11):3612.

58. Shvartsev, B., Cohn, G., Shasha, H., Eichel, R.-A., and Ein-Eli, Y. (2013). Reference electrode assembly and its use in the study of fluorohydrogenate ionic liquid silicon electrochemistry. *Physical Chemistry Chemical Physics*, 15(41):17837–17845.

59. Smets, A., Kessels, W., and Van de Sanden, M. (2003). Vacancies and voids in hydrogenated amorphous silicon. *Applied physics letters*, 82(10):1547–1549.

60. Smets, A. H., Jäger, K., Isabella, O., Swaaij, R. A., and Zeman, M. (2015). *Solar Energy: The physics and engineering of photovoltaic conversion, technologies and systems*. UIT Cambridge.

61. Sriraman, S., Aydil, E. S., and Maroudas, D. (2002). Atomic-scale analysis of deposition and characterization of a-si: H thin films grown from sih radical precursor. *Journal of applied physics*, 92(2):842–852.

62. Sturm, J., Grosse, P., and Theiss, W. (1991). Effective dielectric functions of alkali halide composites and their spectral representation. *Zeitschrift für Physik B Condensed Matter*, 83(3):361–365.

63. Sumirat, I., Ando, Y., and Shimamura, S. (2006). Theoretical consideration of the effect of porosity on thermal conductivity of porous materials. *Journal of Porous Materials*, 13(3-4):439–443.

64. Sun, Y., Liu, X., Jiang, Y., Li, J., Ding, J., Hu, W., and Zhong, C. (2019). Recent advances and challenges in divalent and multivalent metal electrodes for metal–air batteries. *Journal of Materials Chemistry A*, 7(31):18183–18208.

65. Wang, S. (2020). Study of n-type amorphous silicon alloy as the anode in li-ion batteries.

66. Weinrich, H., Durmus, Y. E., Tempel, H., Kungl, H., and Eichel, R.-A. (2019). Silicon and iron as resource-efficient anode materials for ambient-temperature metal-air batteries: a review. *Materials*, 12(13):2134.

67. Wemple, S. (1973). Refractive-index behavior of amorphous semiconductors and glasses. *Physical Review B*, 7(8):3767.

68. Williams, J. T., Vangu, A. M., Mabiala, H. B., Mangungulu, H. B., and Tissingh, E. K. (2021). Toxicity in the supply chain: cobalt, orthopaedics, and the democratic republic of the congo. *The Lancet Planetary Health*, 5(6):e327–e328.

69. Wolf, A., Terheiden, B., and Brendel, R. (2008). Light scattering and diffuse light propagation in sintered porous silicon. *Journal of Applied Physics*, 104(3):033106.

70. Wollam, J. (2011). Completeease data analysis manual. *JA Woollam Co. Inc, New England. United States of America*.

71. Zhang, X. G. (2007). *Electrochemistry of Silicon and its Oxide*. Springer Science & Business Media.

72. Zhao, Y. (2018). Contact stack evaluation for shj solar cells and process development of ibc-shj solar cells.

73. Zhao, Z., Fan, X., Ding, J., Hu, W., Zhong, C., and Lu, J. (2019). Challenges in zinc electrodes for alkaline zinc–air batteries: Obstacles to commercialization. *ACS Energy Letters*, 4(9):2259–2270.

74. Zhong, X., Zhang, H., Liu, Y., Bai, J., Liao, L., Huang, Y., and Duan, X. (2012). High-capacity silicon–air battery in alkaline solution. *ChemSusChem*, 5(1):177–180.

[title=References]